

Submitted for publication in the *Astronomical Journal*.

MOJAVE: Monitoring of Jets in AGN with VLBA Experiments – I. First-Epoch 15 GHz Linear Polarization Images

M. L. Lister

Department of Physics, Purdue University, 525 Northwestern Avenue, West Lafayette, IN 47907

`mlister@physics.purdue.edu`

D. C. Homan

Department of Physics and Astronomy, Denison University, Granville, OH 43023

`homand@denison.edu`

ABSTRACT

We present first-epoch, milliarcsecond-scale linear polarization images at 15 GHz of 133 jets associated with active galactic nuclei (AGN) from the MOJAVE survey. MOJAVE (Monitoring of Jets in Active Galactic Nuclei with VLBA Experiments) is a long-term observational program to study the structure and evolution of relativistic outflows in AGN. The sample consists of all known AGN with galactic latitude $|b| > 2.5^\circ$, J2000 declination greater than -20° , and correlated 15 GHz VLBA flux density exceeding 1.5 Jy (2 Jy for sources below the celestial equator) at any epoch during the period 1994–2003. Of the 133 AGN that satisfy these criteria, 96 are also part of the VLBA 2 cm Survey. Because of strong selection effects, the sample primarily consists of blazars with parsec-scale morphologies consisting of a bright core component at the extreme end of a one-sided jet. At least one third of the cores are completely unresolved on the longest VLBA baselines, indicating brightness temperatures above 10^{11} K. These cores tend to have electric vectors that are better aligned with the inner jet direction, possibly indicating the presence of a stationary shock near the base of the jet. The linear polarization levels of the cores are generally low ($< 5\%$), but many of the extended jet regions display exceedingly high fractional polarizations ($> 50\%$) and electric vectors aligned with the jet ridge line, consistent with optically thin emission from transverse shocks. The cores and jets of the radio galaxies show very little or no linear polarization. Both the weak- and strong-lined blazar classes (BL Lacs and high polarization radio quasars) show a general increase in fractional polarization with distance down the jet, but the BL Lac jets are generally more polarized and have electric vectors preferentially aligned with the local jet direction. We show that these differences are intrinsic to the jets, and not the result of observational biases. We find that distinct features in the jets of gamma-ray loud (EGRET) blazars are typically twice as luminous as those in non-EGRET blazars, and are more highly linearly polarized. These differences can be adequately explained if gamma-ray blazars have higher Doppler boosting factors, as the result of better alignment with the line of sight and/or higher bulk Lorentz factors.

Subject headings: galaxies : active — galaxies : jets — quasars : general — radio continuum : galaxies — BL Lacertae objects : general — polarization

1. INTRODUCTION

In terms of total energy output, active galactic nuclei (AGN) represent some of the most energetic phenomena known in the universe, and provide unique laboratories for studying a variety of high-energy physical processes associated with special and general relativity, particle acceleration, and magnetohydrodynamics. Of particular interest are the roughly 10% of all AGN that generate massive outflows which produce powerful broad-band synchrotron and inverse-Compton radiation. Direct imaging of the radio synchrotron emission from AGN outflows using the Very Long Baseline Array (VLBA) has revealed that they are highly collimated, relativistic jets of material, with apparent superluminal speeds up to $\sim 40 c$ (Jorstad et al. 2001; Kellermann et al. 2004). Images on larger scales show that many are able to remain collimated for hundreds of kiloparsecs before depositing enormous energies ($\sim 10^{61}$ ergs) into large plumes of radio-emitting plasma.

The highly relativistic speeds of AGN jets have a substantial impact on their observed properties, including their apparent speeds, variability timescales, viewing angles, and apparent luminosities. According to a stationary observer, the radiation from a relativistic bulk flow will be highly Doppler-boosted (i.e., beamed) in a forward direction. Any flux-limited sample selected on the basis of this jet emission will therefore preferentially contain jets viewed nearly end-on. For such an orientation, transverse speeds faster than light are possible, and early VLBI observations (e.g., Cohen et al. 1977) were able to detect these apparent superluminal motions in bright, discrete knots that moved outward at steady speed from a stationary “core”, assumed to be associated with an optically thick region near the base of the jet.

The NRAO’s¹ Very Long Baseline Array (VLBA) has radically changed our view of AGN jets, making it possible to routinely obtain high-dynamic range, full polarization images at regular intervals. It is now evident that AGN jets are complex magnetohydrodynamic phenomena that cannot be adequately modeled using simple analytical methods or models involving purely ballistic “knots”. They are best described as highly magnetized fluids that respond to changes in the conditions at their nozzles and in their external environments. The unsuitability of analytical models implies that computer simulations are essential for fully understanding the physics of jet phenomena. Indeed, there are many groups that making important advances in this area (e.g., Hughes, Miller, & Duncan 2002; Koide et al. 2002; Aloy et al. 2003). However, to be effectively applied, these simulations require a large set of observational constraints that are best provided by VLBI arrays, because of their high angular resolution and ability to penetrate through obscuring material in the host galaxies. Although numerous detailed VLBI studies have been made of nearby and unusual individual jets, so far there have been few large statistical studies to investigate the overall properties of the general jet population. In an earlier study using the Pearson-Readhead survey, we demonstrated the advantages in gathering a large amount of data on a small sample (Lister et al. 2001), by identifying several new observational correlations and providing conclusive evidence of relativistic beaming in blazars. However, little could be inferred about the general jet population, because of the small sample size (32 objects) and the presence of complex selection biases. These biases can create artificial correlations in blazar samples and lead to incorrect conclusions. Fortunately, it is possible to properly account for these biases, given a complete sample that is sufficiently large ($\gtrsim 100$ jets), with rigorous selection criteria based on beamed jet emission (Lister & Marscher 1997).

In order to address these issues, we have begun a large, full polarization VLBA campaign on a complete AGN sample with the goal of providing the best possible dataset for investigating the statistical properties

¹The National Radio Astronomy Observatory is a facility of the National Science Foundation operated under cooperative agreement by Associated Universities, Inc.

of AGN jets and modeling their selection biases. MOJAVE, which stands for Monitoring of Jets in AGN with VLBA Experiments, is a complement to the recent VLBA 2 cm Survey (Kellermann et al. 1998; Zensus et al. 2002; Kellermann et al. 2004). The latter program regularly imaged over 150 AGN jets from 1994 to 2002 and made significant discoveries regarding the general kinematics of AGN jets, including the finding that highly superluminal jets are extremely rare, and that the observed pattern speeds are directly connected with the underlying flow. The 2 cm Survey did not, however, investigate the magnetic field evolution of jets, since its observations were of total intensity (Stokes I) only. Also, the survey was drawn from a low-frequency all-sky catalog, and was statistically incomplete from the standpoint of beamed jet emission. As we describe in § 2.1, MOJAVE uses a complete sample selected on the basis of 15 GHz VLBI flux density only.

Although the 2 cm Survey contained the longest continuous monitoring baselines of any VLBI survey carried out to date, reliable speeds could only be measured in roughly 75% of the sources (Kellermann et al. 2004). In the remainder, the angular motions were either too slow (because of low intrinsic speed or high redshift of the host galaxy) or exhibited too few distinct features that could be tracked during the observation interval. Also, a small number of nearby sources displayed very fast motions that were under-sampled by the monitoring intervals. The MOJAVE program is correcting these deficiencies by increasing the monitoring baseline for the slow sources by an additional three years, and sampling the faster sources more frequently. With our current program, we observe each source at intervals ranging from a few months to one year. We will have obtained at least four additional epochs on each source by the end of our program. All of our calibrated data and images are available online at the MOJAVE program homepage².

As MOJAVE is the first multi-epoch VLBI project to provide full linear and circular polarization information on a large sample of AGN jets, many of its goals are statistical in nature. Here we discuss the overall linear polarization characteristics of our sample based on our first-epoch observations only. Details on unusual individual sources, as well as the overall evolution and circular polarization properties of the sample will be presented in subsequent papers.

The overall layout is as follows. In § 2 we discuss the selection criteria and general properties of the MOJAVE sample. In § 3 we describe our observations and data reduction technique, as well as the general method for deriving observational quantities. We discuss the overall polarization characteristics of the sample in § 4, and describe distinct differences in the jets of BL Lac and quasars, as well as gamma-ray and non-gamma-ray-detected blazars. We summarize our main conclusions in § 5.

We adopt a contemporary cosmology with $\Omega_m = 0.3$, $\Omega_\Lambda = 0.7$ and $H_o = 70 \text{ km s}^{-1} \text{ Mpc}^{-1}$. Our position angles are given in degrees east of north, and all fractional polarization quantities refer to linear polarization only. We use the convention $S_\nu \propto \nu^\alpha$ for the spectral index.

2. THE MOJAVE SAMPLE

2.1. Selection criteria

The goals of the MOJAVE program demand a statistically complete AGN jet sample that is bright enough for direct fringe detection with the VLBA, and whose properties can be compared with theoretical models incorporating relativistic beaming effects (e.g., Lister & Marscher 1997). Samples selected via total (single-dish) radio flux density without regard to spectral index are not suitable since they are dominated

²<http://www.physics.purdue.edu/astro/MOJAVE>

by radio galaxies with luminous, extended lobe structure. Their parsec-scale jets are very faint, and imaging them usually requires time-intensive VLBI phase-referencing techniques. Since their jets lie much closer to the plane of the sky than blazars, there is very little Doppler time compression, resulting in much slower evolution and subluminal speeds. Also, simulating the observational biases in such a sample requires detailed knowledge of the relationship between intrinsic jet luminosity and extended lobe power, which is currently not well-constrained.

An approach more suited to our goals involves constructing an AGN sample based on beamed jet emission only. By using the milliarcsecond scale (VLBA) 15 GHz flux density as a selection criterion, one can effectively exclude the contribution from large-scale emission, leaving a sample consisting almost entirely of radio loud AGN with relativistic jets pointed nearly directly at us (i.e., blazars). The only exceptions are a few nearby radio galaxies and several peaked-spectrum sources whose jet axes likely lie much closer to the plane of the sky.

The selection criteria we have chosen for the MOJAVE sample are similar to those of the VLBA 2 cm Survey, and are summarized as follows:

- J2000 declination $\geq -20^\circ$
- Galactic latitude $|b| \geq 2.5^\circ$
- Total 15 GHz VLBA flux density of at least 1.5 Jy (≥ 2 Jy for sources below the celestial equator) *at any epoch* during the period 1994–2003.

Because of the variable nature of strong, compact AGN, we have not limited the flux density criterion to a single fixed epoch. Doing so would have excluded many highly variable sources from the sample, and would subsequently reduce the robustness of statistical tests on source properties.

2.2. Selection method

We have identified a total of 133 AGN that satisfy our selection criteria (see Table 1), 96 of which are also members of the VLBA 2 cm Survey. The procedure used in arriving at this list was somewhat complex because of the limited VLBA monitoring data that were available. Our first step was to compile a candidate list of all known AGN with an observed or extrapolated 15 GHz *single-dish* flux density greater than 1.5/2 Jy. We consulted the Kühn 1 Jy catalog (Kühn et al. 1981; Stickel, Meisenheimer, & Kühn 1994), the VLA calibrator database³, the Parkes Half-Jansky flat spectrum sample (Drinkwater et al. 1997), and the JVAS survey (Browne et al. 2003) for this purpose. The latter is complete to within 2.5° of the galactic plane for northern declinations. Since these combined catalogs are complete over our defined sky region at 5 GHz, the only potentially missing sources at this stage were those AGN with spectra peaked at frequencies higher than 5 GHz, and variable sources that happened to be weak at the time of the catalog selection. To alleviate the former bias, we checked the WMAP catalog (Bennett et al. 2003), the 22 GHz VLBI survey of Moellenbrock et al. (1996), and the high-frequency peaked samples of Teräsranta et al. (2001) and Dallacasa et al. (2000) for sources that met the single-dish flux density criteria. We also added any variable sources from the UMRAO and RATAN AGN monitoring programs (Aller, Aller, & Hughes 2003; Kovalev et al.

³<http://www.vla.nrao.edu/astro/>

2002) that had sufficient 15 GHz flux density at any epoch during the nine-year window. The latter program has observed approximately 3000 radio sources with flux densities exceeding 100 mJy since 1995.

The second stage of source selection was to eliminate from the candidate list all extended sources whose correlated VLBA flux densities were weaker than our cutoff. Past surveys (e.g., the CJF survey, Taylor et al. 1996) have accomplished this by using a spectral flatness criterion, which assumes that the weak-core sources will have steep radio spectra because of their extended structure. We did not adopt this method for our survey, since we found that some nearby AGN with steep spectra but sufficiently bright cores (e.g., M87, 3C 380) were incorrectly rejected. We instead used the measured VLBA flux densities from the VLBA 2 cm Survey as the main criterion for MOJAVE survey membership. If a candidate source still did not meet the VLBI flux density criterion at four different epochs within the time window (or had fewer than four VLBA epochs), we determined the VLBI-to-single dish flux density ratio using near-simultaneous UMRAO and VLBA observations (tabulated in Kovalev et al. 2005). We thus used this to estimate the VLBI 15 GHz flux density based on RATAN or UMRAO observations taken during the nine-year window.

2.3. General properties

In Table 1 we summarize the general properties of the MOJAVE sample. The optical identifications in column (6) are from Véron-Cetty & Véron (2003), with exceptions as noted. The BL Lac objects that Véron-Cetty & Véron (2003) have reclassified as quasars have on occasion displayed emission lines slightly wider than the nominal 5 Å limit. Since these are still much narrower than those typically found in quasars, we retain the BL Lac classifications for these objects. We list the optical V magnitude from Véron-Cetty & Véron (2003) in column (7), and point out that these are highly variable with time. The general descriptions of the radio spectral shape in column (8) are from Kellermann et al. (2004). All but eleven sources have flat overall radio spectra, which we define as a spectral index flatter than -0.5 at any frequency between 0.6 and 22 GHz. The five steep-spectrum sources in the sample have strong extended emission on arcsecond scales that dominates the integrated spectrum, but their parsec-scale emission still meets our selection criteria. The six peaked-spectrum sources have no apparent radio emission on arcsecond scales (with the exception of 2134+004; Stanghellini et al. 1998). We do not include 0738+313 and 1127–145 in the peaked-spectrum category, as they have variable radio spectra that are occasionally flat (Kovalev et al. 2002).

In column (9) of Table 1 we list the strongest measured 15 GHz VLBA flux density during the period 1994–2003. Those values with asterisks are estimated from single-dish measurements as described in § 2.2. Column (10) indicates whether the AGN has been identified as a likely counterpart to a $\gtrsim 30$ MeV gamma-ray source detected by the EGRET instrument on board the Compton Gamma-Ray Observatory. A “Y” indicates a highly probable EGRET identification according to Mattox et al. (2001), Sowards-Emmerd et al. (2003) and Sowards-Emmerd et al. (2004). Hereafter we will refer to these as “EGRET sources”. A “P” indicates a less probable identification according to these authors, and we will refer to these as “probable EGRET sources”. There are some disagreements in the literature regarding these probable EGRET sources, with 0234+285, 1156+295, and 2230+114, being considered as EGRET sources by Mattox et al. (2001), while 0446+112, 0529+483 and 1936–155 are considered as EGRET sources by Sowards-Emmerd et al. (2003, 2004). Mattox et al. (2001) do not consider 0805–077, 1127–145, 1324+224, 1417+385 and 1504–167 to be probable EGRET sources.

An overall summary of the optical and EGRET identifications for the MOJAVE sample is given in Table 2. Optical counterparts have been identified for 93% of the sample, and the redshift data are currently

86% complete. The sample is dominated by quasars, with the weak-lined BL Lacertae objects and radio-galaxies making up 17% and 6% of the sample, respectively.

3. VLBA OBSERVATIONS AND DATA REDUCTION

3.1. Data calibration

The first epoch of MOJAVE observations took place on 2002 May 31 using the Very Long Baseline Array. In this paper we present data obtained from this and ten subsequent 24-hour MOJAVE sessions, up to and including 2004 Feb 11. All 10 VLBA antennas were used at a central observing frequency of 15.366 GHz. The data were recorded in eight baseband channels (IFs) each of 8 MHz bandwidth using 1-bit sampling. Both right and left hand polarizations were recorded simultaneously in IF pairs, giving a total observing bandwidth of 32 MHz in each polarization. During each observing session, short duration (roughly seven minute) scans of 18 MOJAVE sources were interleaved in order to span the widest possible range of hour angle, and to obtain maximum parallactic angle and (u,v) plane coverage. The total integration time on each source was approximately 65 minutes. There was no need to observe any additional calibrators since all the target sources were strong and compact.

The data were edited and calibrated at NRAO and Purdue University following the standard methods described in the AIPS cookbook. The individual IFs were kept separate throughout the processing, and were only averaged together when making the final Stokes images. This was necessary since the polarization leakage terms at each antenna usually differ slightly among the IFs. A total of 80 leakage terms (four IFs times two circular polarization hands, at ten antennas) were determined at each epoch by running the task LPCAL on all sources, and by taking the median solution values after removing obvious outliers. We determined the relative instrumental electric vector position angle (EVPA) rotation between epochs by comparing the individual leakage term solutions over time (Gomez et al. 2002). With very few exceptions, these remained extremely stable over periods of up to a year, and based on the scatter we consider our relative EVPA error between epochs to be less than two degrees. The leakage term method only gives relative EVPA corrections between epochs, and still requires an absolute correction to establish the EVPA directions on the sky. This was obtained by comparing the VLBA EVPAs of the most compact MOJAVE sources with single dish values obtained at the University of Michigan Radio Observatory. The latter observations were carried out typically within a week of the VLBA sessions. The systematic error in the absolute EVPAs is dominated by the non-simultaneity of the observations, and possible polarized structure not sampled by the VLBA. Based on the single-dish comparisons, we estimate that our absolute EVPA values are accurate to within five degrees.

3.2. Imaging

We used the Caltech Difmap package (Shepherd, Pearson, & Taylor 1994) to produce Stokes I, Q and U images of each source from the calibrated visibility data using natural weighting and a cell size of 0.1 milliarcseconds per pixel. The best-fit elliptical Gaussian restoring beam FWHM dimensions varied between 0.45 and 1.5 mas, depending on the declination of the source. The restoring beam parameters are listed in columns (3)–(5) in Table 3. The typical rms noise level, obtained by examining pixels well away from the source in each Stokes I image, was ~ 0.2 mJy beam $^{-1}$. Based on comparisons of highly compact sources to near-simultaneous UMRAO observations, we estimate that the absolute flux density scaling of our VLBA

observations is accurate to within 5%.

In Figure 1 we display the first-epoch 15 GHz VLBA images of the entire MOJAVE sample. Each panel contains two images of the same source, the first consisting of I contours with linear fractional polarization overlaid in color. The latter is defined as P/I , where $P = \sqrt{Q^2 + U^2}$. The second image shows the single lowest I contour plus contours of polarized intensity, and ticks indicating the electric polarization vector directions. In most cases the lowest contour levels correspond to three and five times the rms in I and P, respectively. The linear scale factor of each image in parsecs per milliarcsecond is given in column (12) of Table 3 for those sources with a known redshift.

In columns (6) and (8) of Table 3 we list the total 15 GHz VLBA I and P flux densities of each source. These are determined using the sums of I, Q, and U intensities of all of the pixels shown in Figure 1 whose I intensities exceeded three times the rms noise level of the I image. Using Rayleigh statistics, the noise in the P image was estimated to be 0.66 times the average of the Q and U rms noise levels. If the total P did not exceed five times this value, the latter was used as an upper limit in column (8). The integrated EVPA listed in column (9) is calculated using the total Q and U flux densities of the source, where $EVPA = (1/2) \arctan(U/Q)$.

3.3. Visibility model fitting

From observations of jet phenomena associated with young and evolved stars in our galaxy, as well as nearby AGN jets such as those in M87 and Centaurus A, it is known that these outflows have highly complex three-dimensional structures that do not easily lend themselves to simple statistical analysis. However, the vast majority of AGN lie at extremely large cosmological distances, and many of these details are blurred out by the limited spatial resolution of current ground-based radio interferometers. A close examination of the images in Figure 1 shows several instances (e.g., 0007+106, 0446 + 112, 0642+449, 1751+288) where no actual jet is evident, since it lies below the resolution and/or sensitivity level of the VLBA at this frequency. At the other extreme, there are also cases where the jet is clearly resolved in a transverse direction (e.g., 0836+710, 1641+399, 1828+487), making a more detailed analysis possible. For the statistical purposes of this paper, we have fit each source with a minimum number of elliptical Gaussian “components” that when convolved with the restoring beam, generally reproduce the observed structure. In a separate paper we will present a more detailed ridge line-based analysis of approximately a third of the sample members whose jets are not fully described by multiple Gaussian fits.

We carried out our analysis in the (u,v) plane by fitting the brightest features in each source with two-dimensional Gaussian components. Using the “modelfit” task in DIFMAP, we fit several components to each source, resorting to zero-size (delta-function) points if the least-squares routine shrank the fitted

Fig. 1.— (This figure is available at <http://www.physics.purdue.edu/astro/MOJAVE/paper1/fig1.ps.gz>) First-epoch 15 GHz VLBA images of the MOJAVE AGN sample. Each panel contains two images of the same source, the first consisting of I contours in successive integer powers of two times the lowest contour (see Table 3), with linear fractional polarization overlaid according to the color wedge. A single negative I contour equal to the base contour is also plotted. The second image includes the lowest positive I contour from the first image, and linearly polarized intensity contours, also in increasing powers of two. The sticks indicate the electric polarization vector directions.

Gaussian major axis to extremely small values. These fits provided positions, sizes and flux densities for the brightest, most compact jet features, which are tabulated in Tables 4 and 5. Based on our previous 15 GHz studies (see Appendix A of Homan et al. 2002), we estimate typical errors of 5% on the total intensities and positional errors of $\sim 1/5$ of the restoring beam dimension. For the brightest components, the errors are smaller by approximately a factor of two.

The milliarcsecond morphology of most sources consists of a strong, flat-spectrum “core” component that is typically unresolved along one or both axes of the restoring beam and is located at the extreme end of a more diffuse jet structure. This core component is generally thought to represent the region near the base of the jet where it becomes optically thick. Observational evidence of apparent core shifts with frequency (e.g., Lobanov 1998) support this view.

3.3.1. Core measurements

We list the position of the fitted core component in polar coordinates with respect to the map center in columns (2) and (3) of Table 4. In most cases the core offset is negligible (less than one pixel, or 0.1 milliarcsec), since the phase self-calibration process tends to shift the map center to lie on the brightest feature in the source. Exceptions arise when a strong feature lies very close to the core (e.g., 0224+671), or when the source is dominated by an exceptionally strong feature in the jet (e.g., 0923+392). In sources with a non-zero core offset, there is also the possibility that we are seeing both the jet and the counter-jet. In blazars the latter is not usually visible since its radiation is beamed away from us. There are four sources in our sample in which counter-jets have been detected in other studies: 0316+413 (3C 84), 0238–084 (NGC 1052), 1413+135, and 1957+405 (Cygnus A). The exact location of the core in these sources is not well-defined, because of possible foreground absorption in the vicinity of the central nucleus. In such cases we have considered the feature closest to the map center to be the core. Other sources in our sample which may have visible counter-jets are 0742+103, 1548+056, and 2021+614. Multi-frequency imaging of these AGN would aid in identifying the core based on its predicted flat spectral index, variability, and high brightness temperature. Such a study of 2021+614 is currently underway (Lister et al., in preparation).

The fitted flux density and Gaussian parameters of the core components are given in columns (4) through (7) of Table 4. The brightness temperatures in column (8) are calculated in the observer frame assuming a Gaussian profile using the formula

$$T_b = \frac{1.221 \times 10^{12} S_{core}}{\nu_{obs}^2 a_{maj} a_{min}} \text{ K},$$

where S_{core} is the core flux density in Jy, ν_{obs} is the observing frequency in GHz and a_{maj} and a_{min} are respectively the FWHM major and minor axes of the fitted core Gaussian in milliarcseconds. It should be noted that these are “best-fit” brightness temperatures, and in many cases, may in fact be lower limits because of the limited spatial resolution of the data. For those cores which were completely unresolved along at least one axis of the restoring beam (such that the best fit was a delta-function), a lower limit on T_b was calculated assuming a minimal resolvable component size. The expression for the latter, based on the signal-to-noise ratio at the core position and the restoring beam dimensions, is given by Kovalev et al. (2005).

Columns (9) and (10) list the fractional polarization and EVPA of the core, which are calculated from the mean I, Q, and U of the nine contiguous pixels centered at the fitted core position. In cases where the polarization is below the lowest P contour level listed in Table 2, upper limits are given corresponding to

five times the P rms noise level.

3.3.2. Jet measurements

We use the same Gaussian component method to describe the jet emission in the MOJAVE sample. The results of these fits are given in Table 5. Additionally, we measure the mean jet polarization by integrating over all jet emission. This is determined in the image plane using only those pixels that are above the base I contour level listed in Table 1. We exclude pixels in the core region defined as

$$\left(\frac{x}{b_{min}}\right)^2 + \left(\frac{y}{b_{maj}}\right)^2 \leq \frac{\ln |I_{core}/I_{base}|}{4 \ln 2},$$

where b_{maj} and b_{min} are the FWHM major and minor axes of the Gaussian restoring beam, and x and y are the right ascension and declination coordinates of the pixel with respect to the core. I_{base} is the lowest contour level in the image and I_{core} is the pixel intensity at the core position. Outside this region, the emission from the core is below the lowest contour level. For most sources, it corresponds to an ellipse with dimensions approximately equal to those of the Gaussian restoring beam listed in Table 3.

4. DISCUSSION

4.1. Core component properties

Although the flat-spectrum core components are responsible for much of the polarized and total flux density in our VLBA images, their properties are the most difficult to interpret because they likely represent a blend of many small individual emitting regions close to the base of the jet. In roughly one third of the sources, the core feature could be adequately fit by an unresolved point model, yielding only a lower limit on the brightness temperature. The observed brightness temperatures of the remaining sources are typically above 10^{11} K, which is close to the detection limit of ground-based interferometers for cores with flux densities of a few hundred mJy. For this reason we expect that many of the T_b values listed in Table 4 are also lower limits. Indeed, a full (u, v) plane analysis of the fine-scale structure of 250 flat-spectrum AGN in the MOJAVE and 2 cm Survey samples by Kovalev et al. (2005) shows that in over 65% of the sources, at least half of the total flux density is unresolved on the longest baselines.

The relative prominence of the core component with respect to the remainder of the VLBI jet varies significantly among the sources in our sample. We define the core-to-jet flux density ratio as

$$R_j = \frac{S_{core}}{S_{jet}(1+z)^{0.7}},$$

where we have assumed typical spectral indices of 0 and -0.7 for the core and jet, respectively. For sources without measured redshifts we assume a typical value of $z = 1$. The distribution of R_j (Figure 2) is very broad, spanning four orders of magnitude, with a peak at approximately $R_j = 3$. The spread in R_j is likely a result of strong flux variability in the core components, as well as a wide range of Doppler factor in the jet population. The latter broadens the distribution since the core and jet emission, having different spectral indices, are expected to be beamed by different amounts. We do not find R_j to be correlated with either redshift or angular size distance.

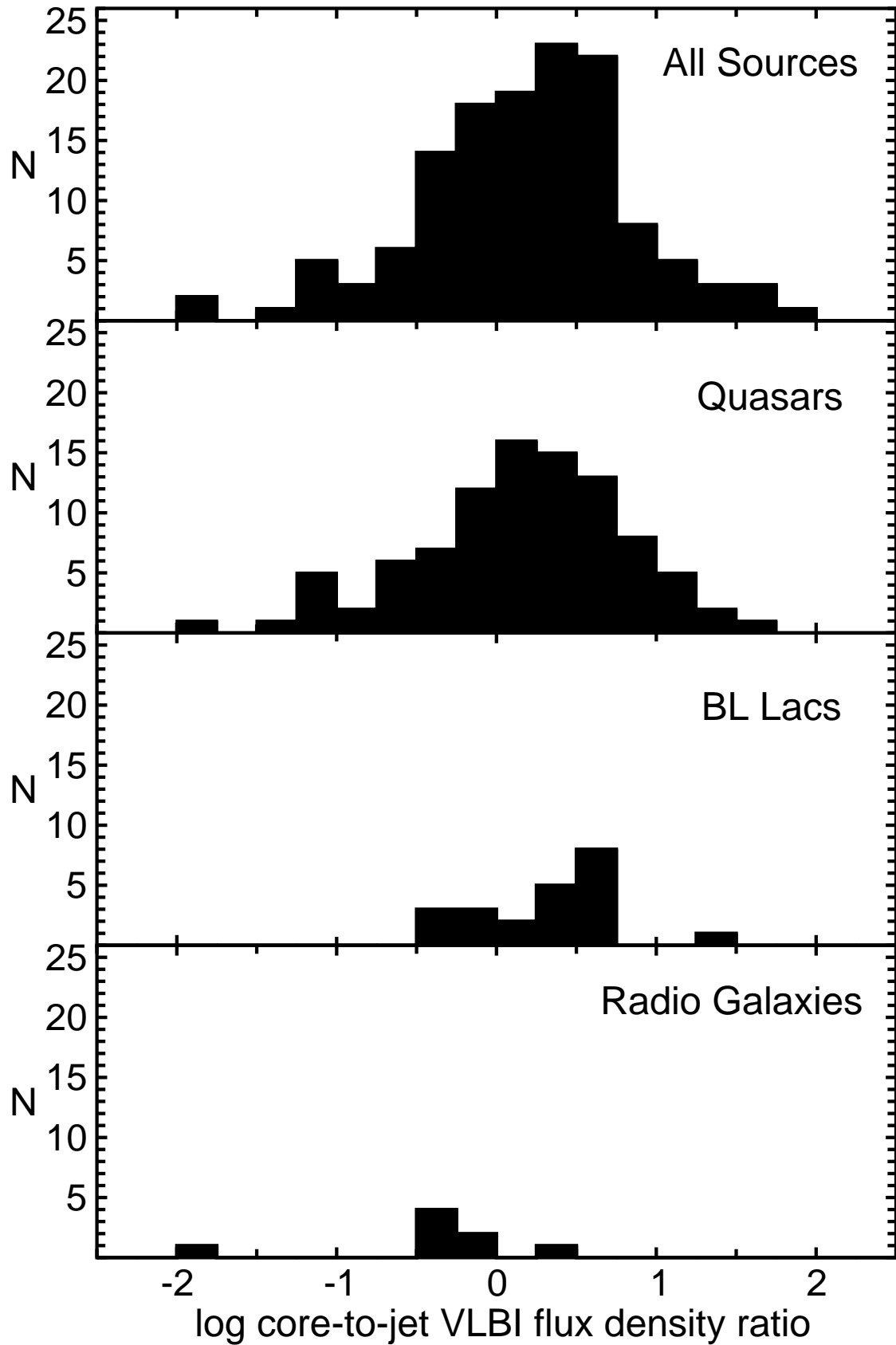


Fig. 2.— Distribution of VLBI core-to-jet ratio (R_j) for the full MOJAVE sample (top panel), and major optical subclasses (lower panels).

The core components have typically low fractional polarizations ($m_{core} \lesssim 5\%$), and range up to a maximum of $\sim 10\%$ in the case of 1538 + 149 (Fig. 3). No polarized emission was detected in any of the eight radio galaxy cores. This was also the case for seven quasars and one BL Lac object (1413+135). As we discuss in § 4.2, the fractional polarization levels are generally much higher in jet regions downstream from the core.

The linearly polarized emission may be strongly depolarized in the core regions, either from an external screen or internal plasma processes. This would also imply a random rotation of the observed electric vectors with respect to the jet, however, this is not the case for the BL Lacertae cores (Figure 4). The latter tend to have core electric vectors that are well-aligned with the inner jet direction. Faraday depolarization without accompanying rotation is possible, but typically requires special geometries that include a mixture of Faraday thin and thick material on scales smaller than the restoring beam. Some quasars are known to have large parsec-scale rotation measures (Zavala & Taylor 2004), but there are currently not enough data to indicate whether there are strong differences in the Faraday screens of weak- and strong-lined blazars. If such differences do exist, they must persist out to several hundred parsecs out from the central engine, since we show in § 4.3.2 that these polarization differences are also present in jet regions well downstream from the cores.

The case for Faraday depolarization is much stronger in the seven sources in our sample for which very little or no polarized emission is present in our images. The jets of the radio galaxies 0007+106, NGC 1052, M87, Cygnus A, and 2021+614 lie at larger viewing angles, and are heavily depolarized by material associated with an obscuring torus located in their host galaxies. The two remaining unpolarized sources, the BL Lac object 1413+135 (Perlman et al. 2002) and the peaked-spectrum quasar 0742+103 (Best et al. 2003), also display heavy absorption features in their central regions. The nearby radio galaxy 3C 84 also suffers from heavy foreground absorption (Walker et al. 2000), and we detect polarized emission only in the southern lobe that is presumably located closer to us (Figure 1).

Apart from possible Faraday depolarization, the cores may appear weakly polarized because of optical depth effects. Synchrotron radiation from an optically thick region such as the core will tend to be weakly polarized because the fields are usually not well-ordered over the short path length into the plasma (Hughes 2005). Also, if the core region contains regions of orthogonal electric vectors, these can combine within the VLBI restoring beam to lower the net polarization. We find a tendency for the most unresolved cores (those with only lower limits on brightness temperature) to have electric vectors that are better aligned with the inner jet direction (Figure 5). Such an alignment might be expected, for example, from a strong standing shock near the base of the jet. The misaligned cases may simply be instances where we have insufficient spatial resolution to separate one or more components close to the base of the jet. Since such features will eventually propagate downstream, it will be possible to investigate this scenario more fully using the full multi-epoch MOJAVE polarization dataset.

4.2. Jet properties

At least 94% of the MOJAVE sources have one-sided jet morphologies, which is a strong reflection of the sample selection biases. If the milliarcsecond-scale emission from these jets is highly anisotropic (i.e., beamed along the flow direction), the sources with the highest flux densities will tend to have their jet axes preferentially aligned toward the observer. Emission from the receding jet will be beamed in the opposite direction, rendering it nearly undetectable. This tendency toward one-sided jets is well-known from previous

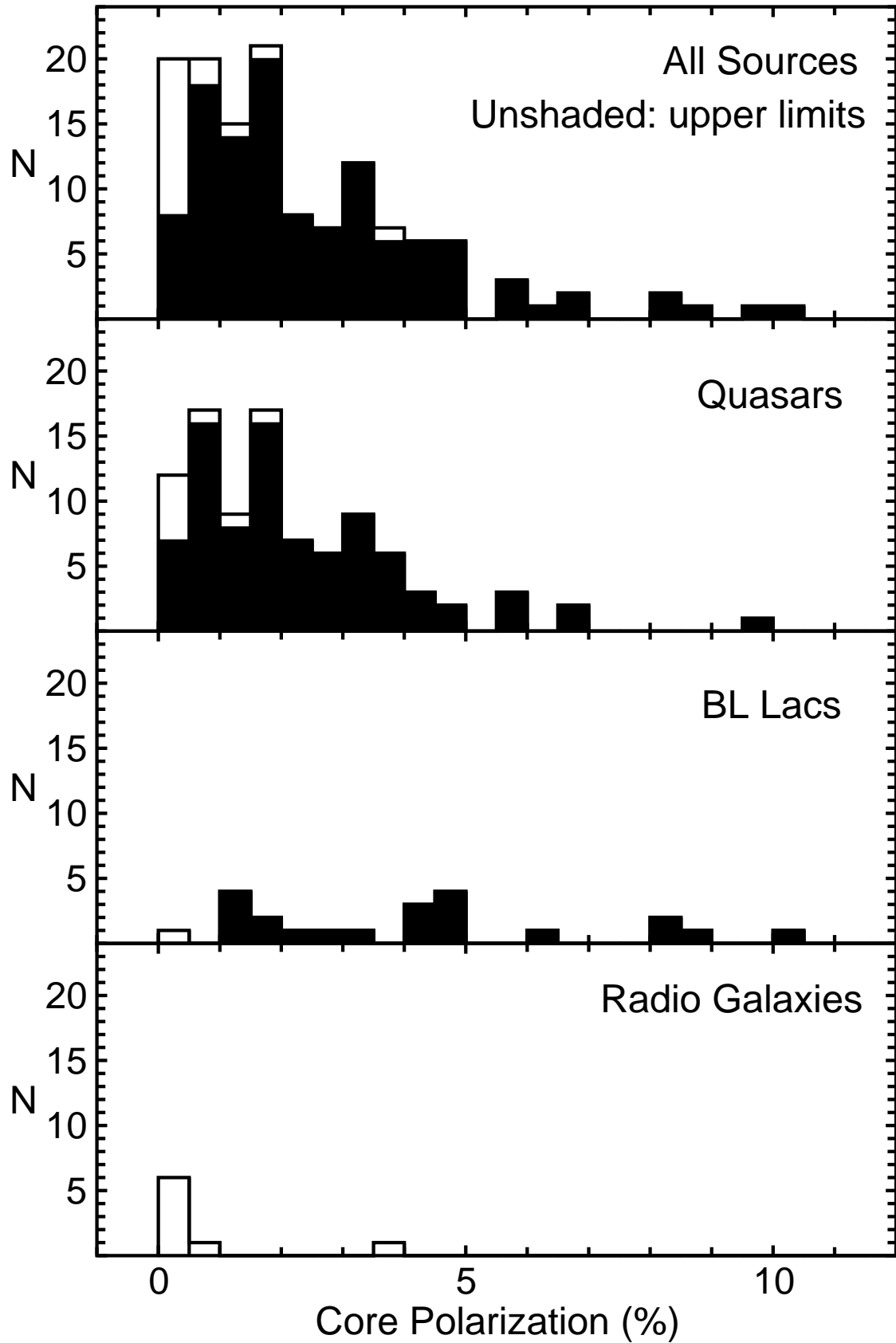


Fig. 3.— Linear fractional polarization of the VLBI core component for the entire MOJAVE sample (top panel) and three major optical subclasses (lower panels). The unshaded boxes represent upper limits on those cores in which no linear polarization was detected. The distribution for the BL Lacs differs from the

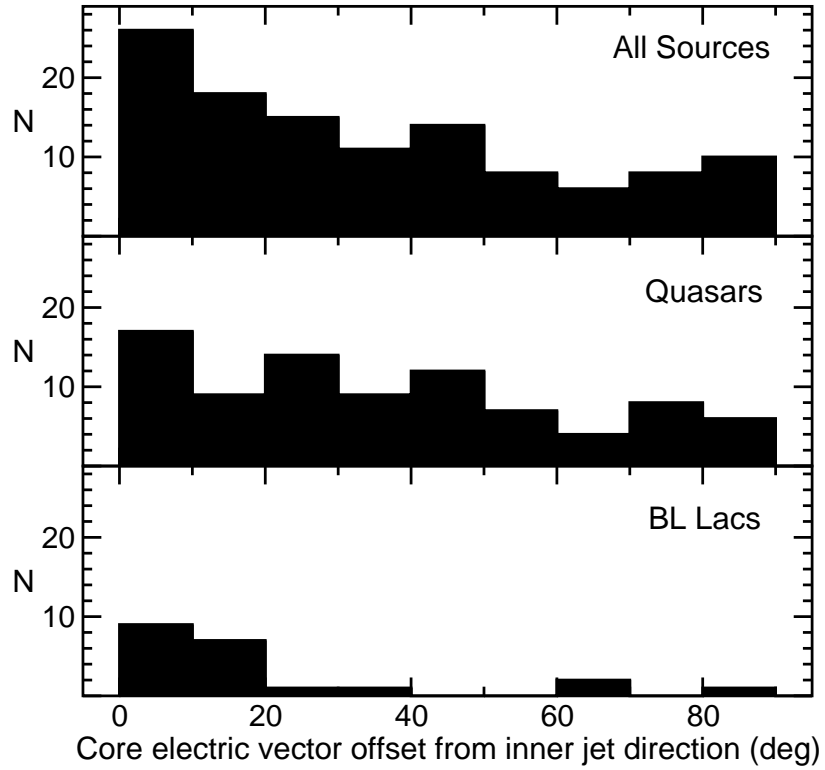


Fig. 4.— Distribution of electric vector offset with respect to inner jet direction at the locations of VLBI cores in the MOJAVE sample. The inner jet direction is defined as the position angle of the Gaussian jet component closest to the core. The BL Lac and quasar distributions differ at the 99.9% confidence level according to a K-S test.

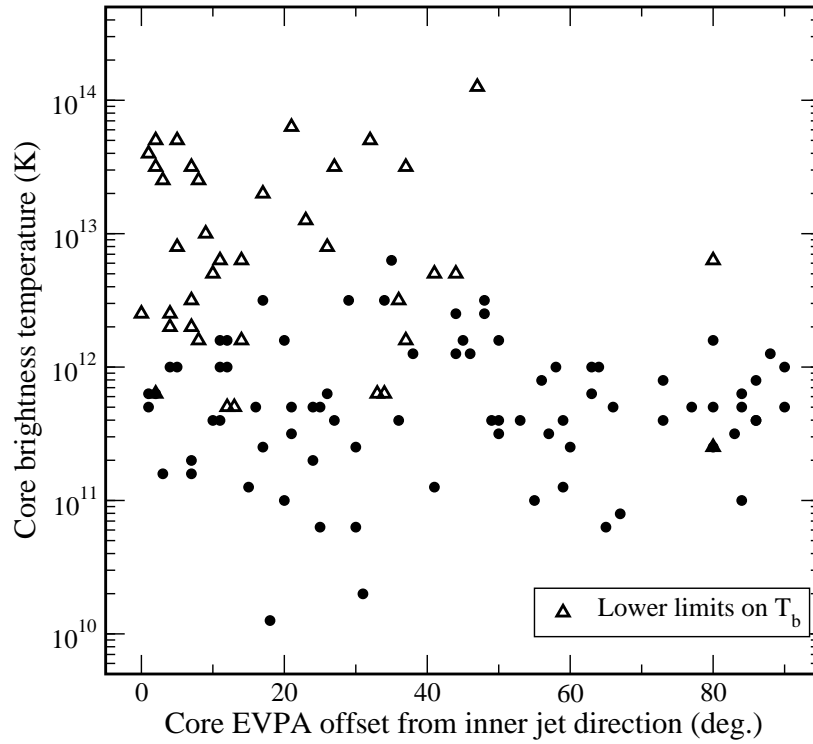


Fig. 5.— Observed brightness temperature versus electric vector misalignment angle for core components in the MOJAVE sample. The filled circles denote best-fit brightness temperatures, and the open triangles denote lower limits. Cores with the highest brightness temperatures tend to have electric vectors that are better aligned with the inner jet direction.

VLBI surveys (see review by Urry & Padovani 1995), and is considered to be key evidence for relativistic bulk motion in AGN jets.

There are still two ways that lesser-aligned jets (lying closer to the plane of the sky) can meet the MOJAVE selection criteria and yet appear as two-sided. They may have a) sufficient flux density merely because of their proximity (e.g., NGC 1052, Cyg A, 3C 84), or b) sufficiently small intrinsic size that their (isotropic) lobe emission dominates their milliarcsecond-scale flux. Some of the peaked-spectrum radio sources, believed to be young jets, fall into this category. Possible examples in MOJAVE include 0742+103 and 2021+614.

Despite the large amount of foreshortening caused by the orientation bias of the MOJAVE sample, we still find several major trends in the observed jet properties. In Figure 6 we plot the linear fractional polarization of fitted jet components against their projected distance from the core in parsecs. Ignoring the artificial trend of the upper limits getting larger with distance (because of the weakening flux density of the jet components), there is a clear upward trend of fractional polarization, which is confirmed by Kendall’s tau test on censored data at greater than 99.99% confidence. This increase in polarization with distance downstream has also been seen in smaller samples at 5 GHz (Cawthorne et al. 1993), 15 GHz (Homan et al. 2002), 22 GHz (Lister & Smith 2000), and 43 GHz (Lister 2001). The polarizations at the sites of the fitted Gaussians range up to a maximum of $\sim 40\%$ seen in 3C 279 (1253–055), with more typical values of $\sim 5\%$. However, in many jets the maximum in fractional polarization does not occur at the locations of fitted components, with some regions being more than 50% linearly polarized (Fig. 1). Such high values indicate extremely well-ordered fields in optically thin synchrotron-emitting regions, and can potentially be used to constrain the viewing angle to the jet (e.g., Cawthorne & Wardle 1988).

The EVPA orientations of the jet components lie at a variety of angles to the local jet direction, which we define as the direction to the nearest component upstream (Fig. 7). The distribution of EVPA offset is peaked at zero degrees, indicating an excess of jet components with electric vectors aligned with the jet. Assuming that the jet components are optically thin and that the magnetic field lies perpendicular to the observed electric field vectors, the form of the distribution is similar to that predicted for an ensemble of oblique shocks with random orientations within the jet (Lister, Marscher, & Gear 1998). Transverse shocks aligned with the flow always have EVPA offsets of zero, regardless of observer viewing angle (Cawthorne & Cobb 1990), so these cannot be dominant in quasar jets. There is no overall trend between the EVPA offset and projected distance from the core as seen by Lister & Smith (2000) at 43 GHz. Our observations are probing regions much further downstream at poorer spatial resolution, however, and the steep fall-off in jet intensity typically prevents polarized emission from being detected in the outermost components.

4.3. Connections with optical emission line properties

There are now several studies (Cawthorne et al. 1993; Lister, Marscher, & Gear 1998; Lister 2001) that have found substantial differences in the parsec-scale polarization properties of weak- versus strong-lined blazars. These AGN classes are commonly referred to as high-polarization radio quasars (HPRQ) and BL Lacertae objects, respectively, with the division occurring at a rest-frame equivalent emission line width of 5\AA . This number is somewhat arbitrary, since historically there has been little evidence for any bi-modality in the emission line width distribution of radio-loud AGN, although Landt et al. 2004 have proposed a new classification scheme based on a bi-modality of O[III] line width. Furthermore, the duty cycles of emission line variability are not well known, making the BL Lac classification of individual objects often controversial.

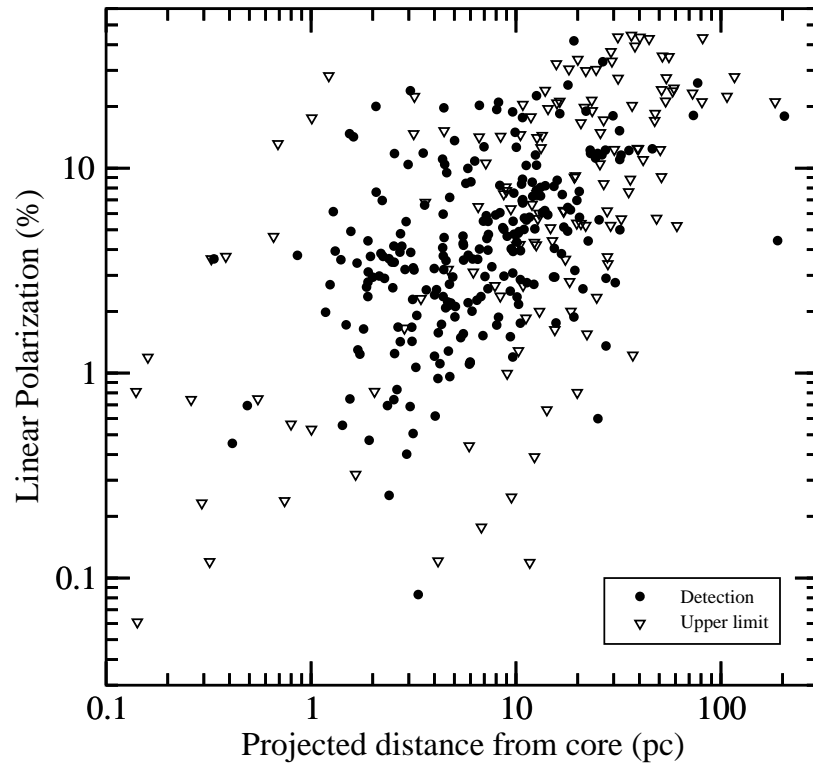


Fig. 6.— Plot of linear fractional polarization of individual jet components versus projected distance from the VLBI core component. The filled circles indicate polarization detections, while the open triangles represent upper limits.

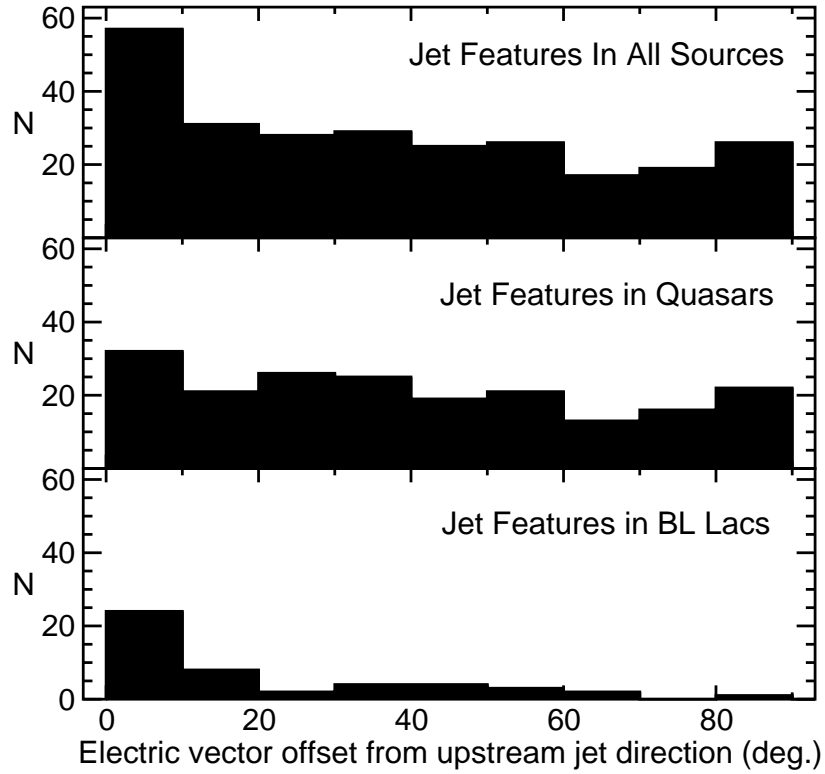


Fig. 7.— Distribution of electric vector offset with respect to the upstream jet direction at the locations of jet components in the full MOJAVE sample (top panel), and for optical subclasses (lower panels). The upstream jet direction is defined as the position angle to the nearest component located closer to the core. The BL Lac and quasar distributions differ at greater than 99.99% confidence according to a Wilcoxon test.

Given these caveats, we use the most prevalent BL Lac and quasar classifications found in the literature (see Table 1) to re-examine the possible differences in the parsec-scale jets of these two optical classes using a large, complete blazar sample. For quantities that do not involve limits, we use the Kolmogorov-Smirnov (K-S) test, and for censored quantities we use Gehan’s generalized Wilcoxon test from the ASURV survival analysis package (Lavalley et al. 1992).

4.3.1. Core component properties

We find the VLBI core components of BL Lacs to be typically more polarized than the quasars (Fig. 3). They also have electric vectors preferentially aligned with the inner jet direction, whereas the quasar cores show no preferred E-vector orientation (Fig. 4). Although the median core-to-jet ratio for BL Lacs appears to be slightly higher than the quasars (Fig. 2), the K-S test only gives a 89% probability that the two are drawn from different parent distributions.

4.3.2. Jet properties

Lister (2001) found that at 43 GHz, the jets of BL Lac objects in the Pearson-Readhead sample tend to be more polarized at a given projected distance from the core than those of quasars. We confirm these findings using the much larger MOJAVE sample at 15 GHz. At our lower observing frequency, it is possible to image much more of the faint, steep-spectrum regions located further down the jet, at the expense of poorer spatial resolution. In Figure 8 we plot fractional polarization versus projected angular distance from the core for all jet components in the MOJAVE sample with detected polarized emission. Although the BL Lac jet components are spread over a large region of the diagram, most lie near the top of the distribution, as also seen at 43 GHz by Lister (2001). The jet components of BL Lacs are not only more polarized than quasars (Fig. 9) but also have electric vectors preferentially aligned with the ridge line (Fig. 7).

4.3.3. Possible luminosity and redshift biases

One possible explanation for the polarization differences in quasars and BL Lacs is that the latter are preferentially located at lower redshifts, and therefore have lower luminosities in our flux-limited sample. In Figure 10 we show a plot of maximum total 15 GHz VLBI luminosity versus redshift for the optically identified objects in the MOJAVE sample. K-S tests indicate that the BL Lacs are concentrated in a different region of the L-z plane than the quasars.

As a check on possible biases in our analysis, we re-performed our statistical tests on sub-samples that included only those BL Lacs and quasars with maximum 15 GHz VLBI luminosity greater than $8 \times 10^{26} \text{ W Hz}^{-1}$. The BL Lacs without known redshifts were also included. We selected a subsample of 48 quasars that closely matched the $L - z$ region occupied by the BL Lacs, such that the two redshift, angular size distance, and maximum 15 GHz VLBI luminosity distributions were not statistically different according to a K-S test. We verified that the core and jet luminosity distributions of the two subsamples were also statistically indistinguishable.

We find that the differences in polarization between the two optical classes are still present in these matched samples, with drops in confidence level of less than 1%, mainly as a result of the smaller sample

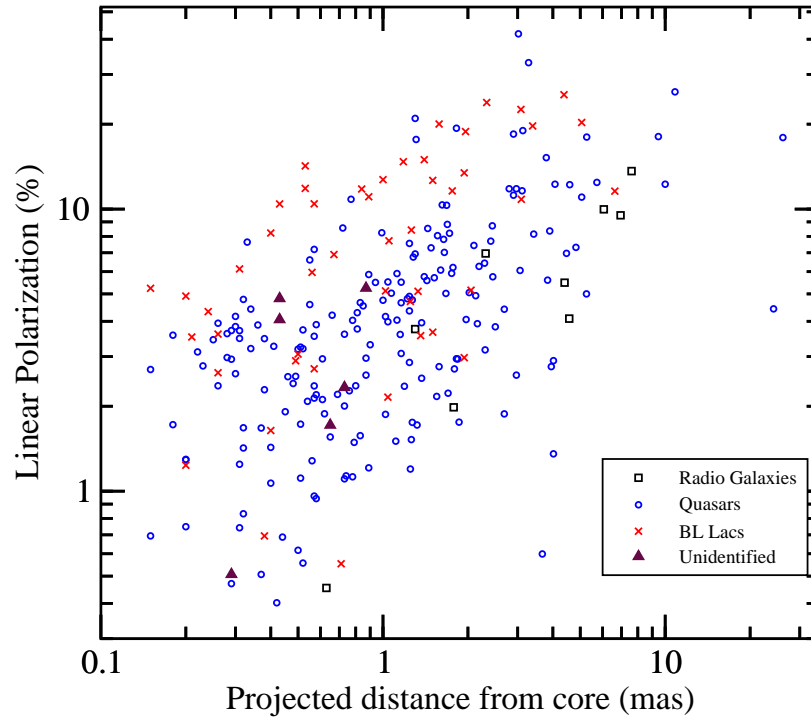


Fig. 8.— Plot of linear fractional polarization of individual polarized jet components versus angular projected distance from the VLBI core component. The open circles and squares denote those associated with quasars and radio galaxies, respectively, while the crosses denote those associated with BL Lac objects. The open triangles belong to jets with no known optical counterparts.

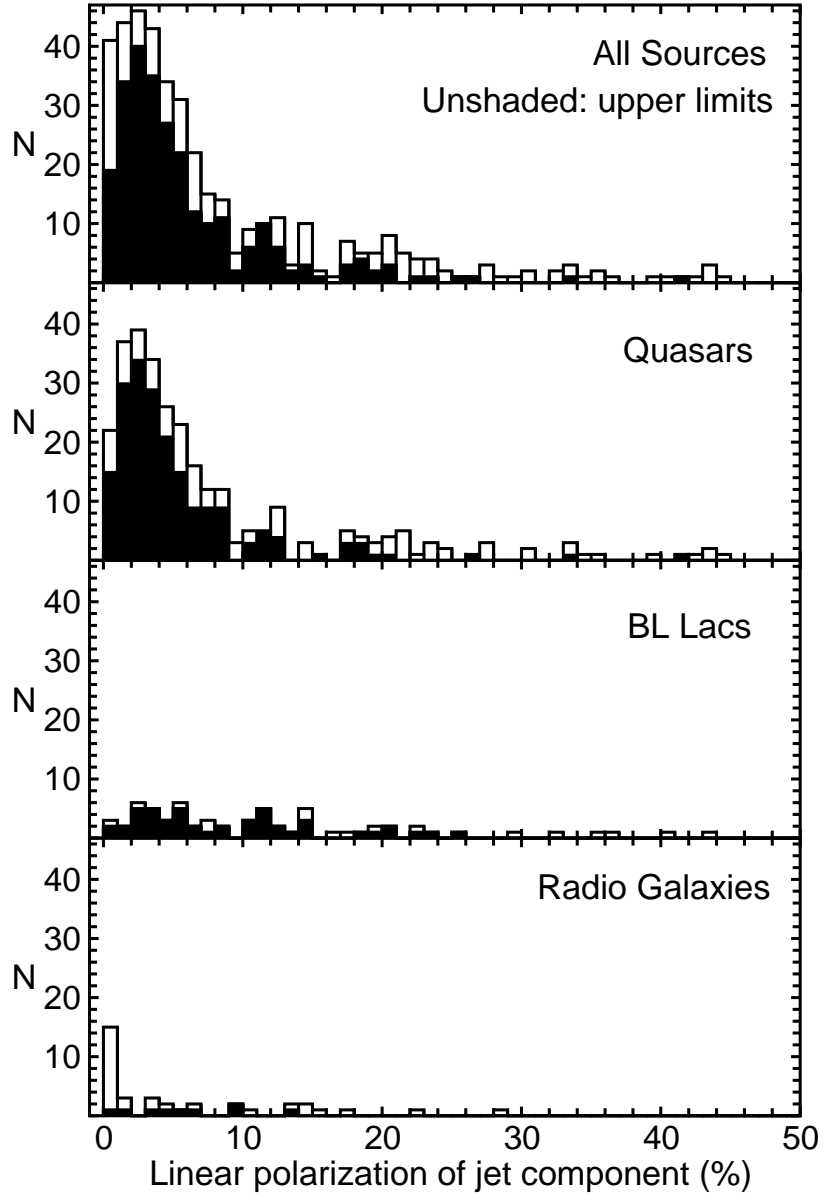


Fig. 9.— Distributions of linear fractional polarization for jet components in the full MOJAVE sample (top panel), and optical sub-classes (lower panels). The unshaded boxes represent upper limits for those components with no detected polarization. The quasar and BL Lac distributions differ at greater than 99.99% confidence according to a Wilcoxon test.

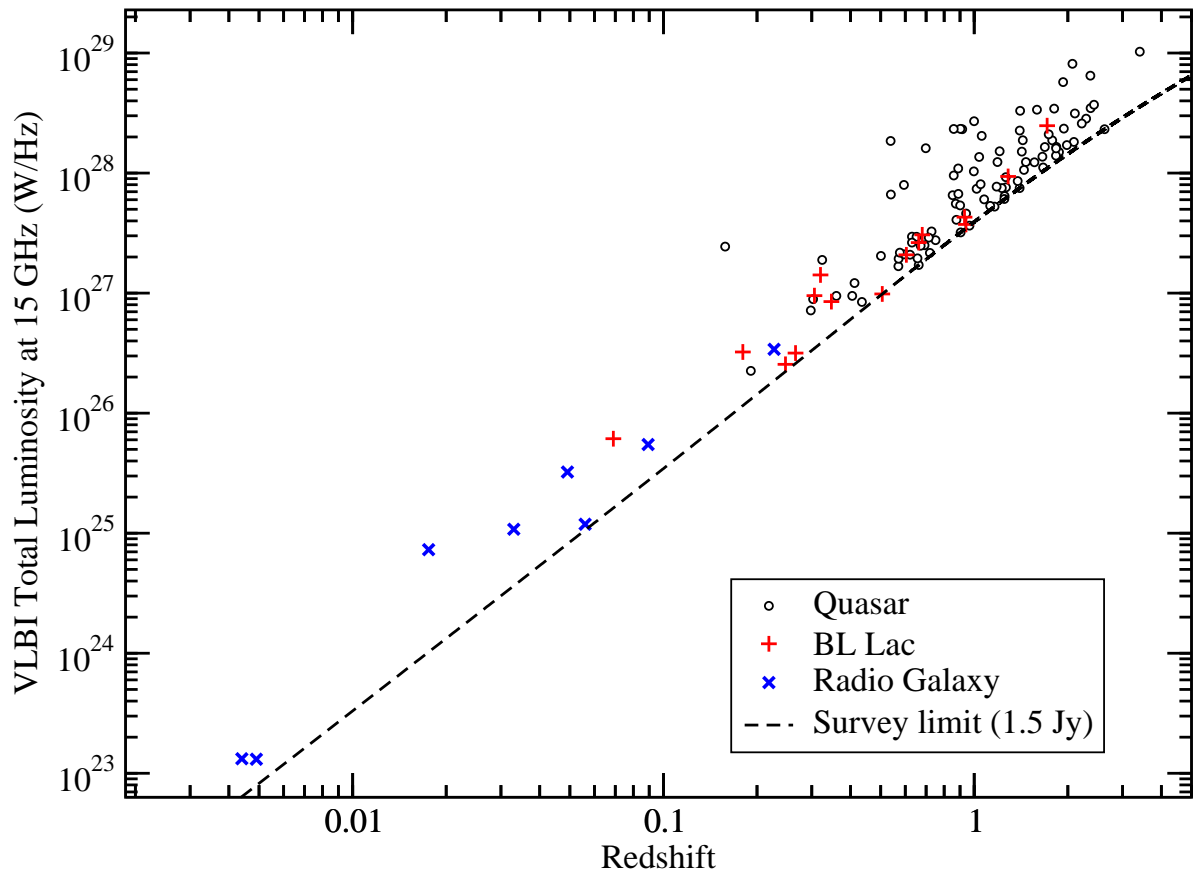


Fig. 10.— Maximum 15 GHz total VLBI luminosity versus redshift for optically identified MOJAVE sources. The dashed line corresponds to the survey limit of 1.5 Jy for northern sources, assuming flat radio spectra. The open circles denote quasars, the plus symbols denote BL Lac objects, and the x's represent radio galaxies.

sizes. Therefore, the differences cannot be attributed to luminosity bias. The presence of these apparent differences at both 15 and 43 GHz argues against Faraday screens being the culprit, unless the rotation measures are exceptionally high. The fact that many polarized jet regions with $m > 10\%$ are seen in both BL Lacs and quasars suggests that this is unlikely.

Our observations therefore indicate that the magnetic field properties of BL Lac and quasar jets are intrinsically different, either as a result of internal properties, such as jet power or speed, or the external environment through which the jet is propagating. There is already evidence that BL Lac jets may be the beamed versions of low-power FR-I type radio galaxies, while quasars are associated with FR-II sources (Urry & Padovani 1995). Numerical simulations suggest that strong shocks form more easily in low-Mach number flows (P. Hughes, private communication). In this case, BL Lac jets may preferentially contain strong, transverse shocks that increase the field order to a higher degree than weaker, oblique shocks that develop more frequently in the jets of quasars. Another possibility, raised by Jorstad et al. (2005), is that forward and reverse shocks may have fundamentally different polarization properties, with the latter being more prevalent in BL Lac objects.

4.4. Connections with gamma-ray properties

During its years of operation between 1991 to 1995, the EGRET instrument on board the Compton Observatory detected approximately 60 blazars at energies above ~ 30 MeV. There has been much discussion as to whether these “EGRET blazars” are intrinsically different in some respect from the general blazar population. Gamma-ray emission models involving inverse-Compton scattering (e.g., Dermer, Schlickeiser, & Mastichiadis 1992) suggest that the gamma-rays are highly relativistically beamed, perhaps much more so than the radio synchrotron emission. It has been suggested that the blazars detected by EGRET have particularly high Doppler factors (Lähteenmäki & Valtaoja 2003), and kinematic studies (Kellermann et al. 2004) have indeed shown that they have faster superluminal jet speeds. This simple picture is complicated, however, by the highly variable nature of AGN at all wavelengths, particularly in gamma-rays, where rapid, energetic flaring events have been detected in many sources. The production of large gamma-ray flares in blazars appears to be closely connected with activity in the parsec-scale jets. Lähteenmäki & Valtaoja (2003) established a connection between flare activity at gamma-ray and mm-wave energies, and Jorstad et al. (2001) have reported that gamma-ray flares are often associated with the appearance of new, superluminal features in the parsec scale jet.

The MOJAVE sample offers a new means of comparing the parsec-scale jets of EGRET and non-EGRET sources, since it is selected on the basis of compact radio flux density and is not biased with respect to gamma-ray flux. It contains 26 AGN considered to be “high-probability” EGRET identifications by Mattox et al. (2001) and Sowards-Emmerd et al. (2003, 2004), as well as 12 “probable” identifications. We have divided the MOJAVE sample according to these EGRET classifications (listed in Table 1) and performed standard statistical tests on various properties to see if they originate from the same parent population. For the purposes of our tests we have grouped the “probable” identifications into the EGRET blazar class.

We find that the EGRET and non-EGRET blazars have statistically indistinguishable optical magnitude and redshift distributions. There is a marginal difference in the total 15 GHz VLBA luminosity distributions (94% confidence), which increases to 99% confidence if the probable-EGRET sources are counted instead as non-EGRET blazars. There is also a marginal indication (93% confidence) of a difference in the core luminosity distributions. Clear differences are present in the parsec-scale jet features. In Figure 11 we

show the 15 GHz luminosity distribution of all the Gaussian components fitted to the MOJAVE sample, subdivided according to gamma-ray classification. The median component luminosity in gamma-ray blazar jets is twice that of the non-EGRET blazars, and the K-S test gives only a 0.3% chance that the luminosities are drawn from the same parent distribution.

The jets in EGRET sources also have statistically higher fractional polarization levels, with a mean integrated jet polarization of 3.6% compared to 2.3% for non-EGRET sources. A survival analysis comparison of the jet polarization distributions (Fig. 12) indicates a difference at the 95% confidence level (99.99% if the probable EGRET sources are reclassified as non-EGRET). This is also the case for the polarization distributions of individual jet components (Fig. 13). Considering the distributions of polarization detections alone, the differences in the two classes are not large, however, the distribution of upper limits in Fig. 13 indicates that the gamma-ray blazar jets are more highly polarized overall. Unlike the case of BL Lacs versus quasars, we see no tendency for EGRET jets to be more polarized at a given distance from the core than non-EGRET jets.

These differences are perhaps unexpected, since they occur tens to hundreds of parsecs downstream of the region where most models suggest the gamma-rays are produced (near the base of the jet). It is possible that the correlated jet and gamma-ray properties of the MOJAVE blazars are not intrinsic to the jets, but are instead induced by Doppler effects. EGRET blazars display a wider range of superluminal speeds (Kellermann et al. 2004), which could imply that they have higher Lorentz factors and/or jet axes aligned more closely with the line of the sight. This would boost the apparent luminosity of their finite-lifetime, steep-spectrum jet features more than their non-gamma-ray counterparts. To reproduce the factor of two seen in the MOJAVE sample, a difference in viewing angle of only 3 degrees is needed, assuming a Lorentz factor of 10 and a spectral index of -0.7 . This number increases to approximately 10 degrees for a Lorentz factor of 3. Such differences in viewing angle may have a large effect on observed polarization detections, since orthogonally-polarized regions may become blended via projection effects, effectively canceling their polarized signal. Also, for high Lorentz factor flows, a small change in viewing angle can translate into a large change in aberrated angle in the jet rest frame, leading to different levels of observed polarization (Hughes, Aller, & Aller 1985). It is not clear how the observed jet electric vectors are affected in detail by viewing angle changes, since this depends largely on the mechanism that produces the polarization. If the polarization is from strong, transverse shocks, the E-vectors should always align with the jet flow. Unlike the case of BL Lacs versus quasars, we find no differences in the electric vector offset distributions of the EGRET versus non-EGRET sources, which argues against intrinsic magnetic field differences.

Since the observed EGRET/non-EGRET polarization differences are substantially different than those seen between BL Lacs and quasars, more than one mechanism is probably at work. A Fisher’s exact test on Table 2 shows no indication that the gamma-ray properties of MOJAVE sources are related to their optical properties (i.e., gamma-ray detections do not favor quasars over BL Lacs). BL Lacs show strong indications of a dramatically different magnetic field structure than quasars, perhaps as a consequence of lower jet power.

Although the Doppler factor scenario appears to account for the differences in gamma-ray blazar jet properties, it would also suggest that these should extend to the core components. We only find a marginal difference in the core luminosities of EGRET versus non-EGRET blazars, and no differences in the core polarization properties. The core luminosity may depend less strongly on Doppler factor because of its flat spectral index and the fact that its emitting plasma is likely to be continuously re-supplied (e.g., Lind & Blandford 1985). But as pointed out by Lister (2001), the relation may not be not straightforward, since it must take into consideration inverse-Compton losses, finite lifetimes of unresolved components, and possible deceleration of the flow. It is also possible that the high variability level of the cores is masking any differences

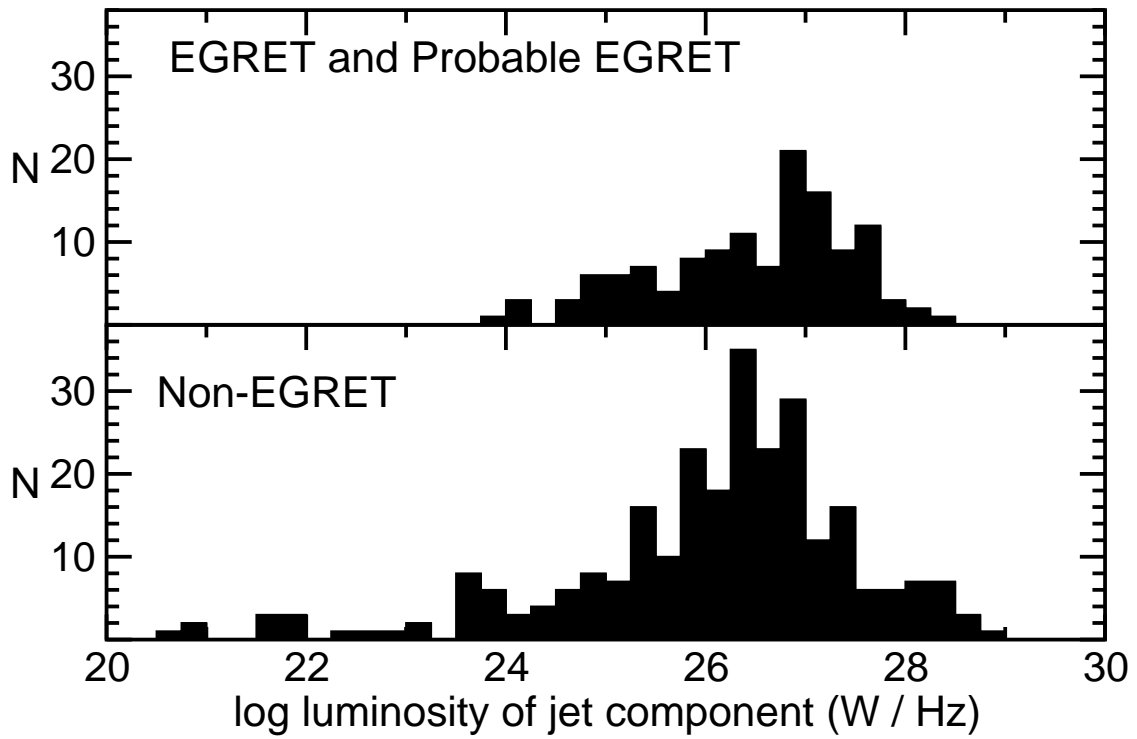


Fig. 11.— Distribution of luminosity at 15 GHz for individual jet components in gamma-ray (EGRET-detected) AGN (top panel), and non-EGRET AGN (lower panel) in the MOJAVE sample.

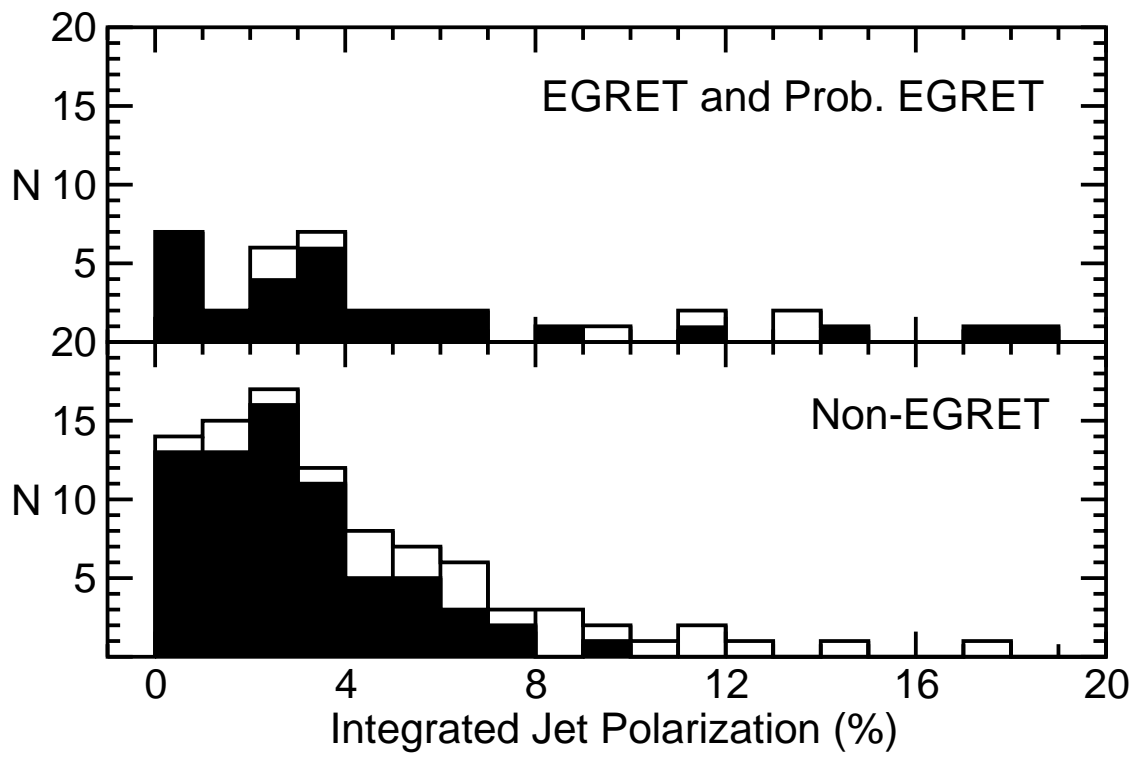


Fig. 12.— Distribution of integrated fractional polarization for the jets of EGRET (top panel) and non-EGRET (lower panel) AGN in the MOJAVE sample.

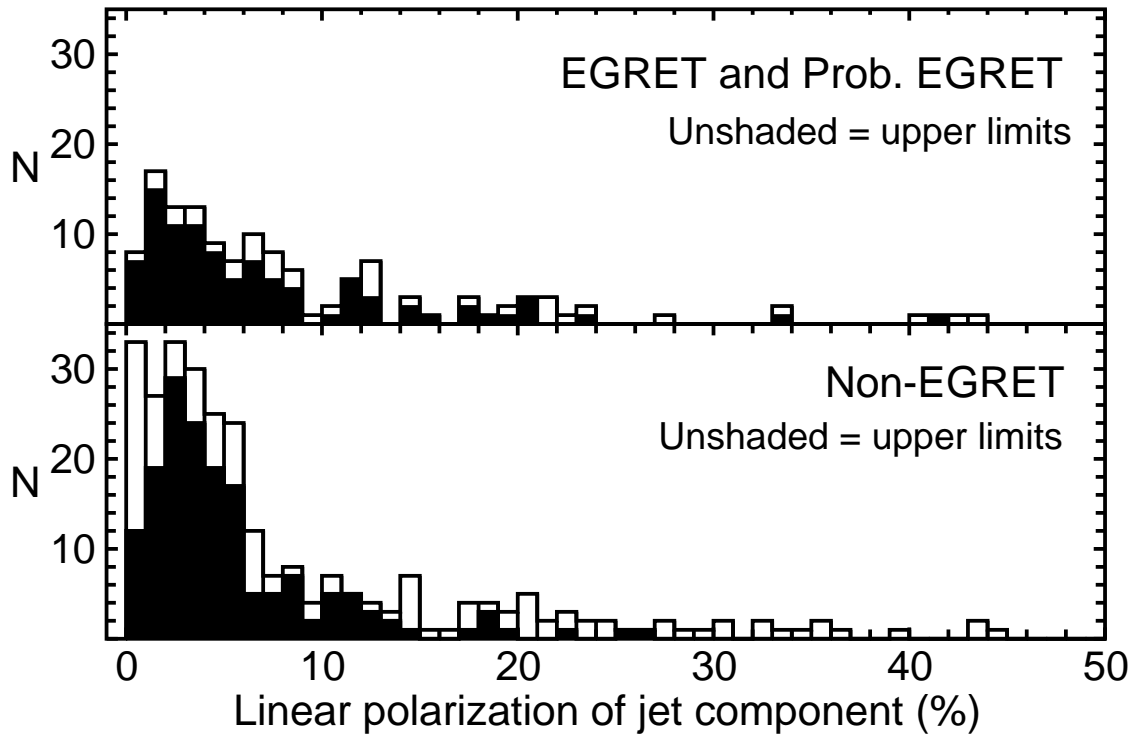


Fig. 13.— Distribution of fractional polarization for individual components in the jets of EGRET (top panel) and non-EGRET (lower panel) AGN in the MOJAVE sample. The two distributions differ at the 99.9% confidence level according to a Kendall’s tau test on censored data.

in our single-epoch dataset.

As a further test of our hypothesis, we have divided the component luminosities by the core luminosity in each source and applied k-corrections using typical spectral indices of zero and -0.7 for the core and jet, respectively. When comparing these “normalized” component luminosities in which the dependence on Doppler factor has been reduced, we find no statistical differences between the EGRET and non-EGRET sources, thereby supporting our scenario.

In summary, the jet properties of gamma-ray blazars investigated here can be reconciled by assuming that they have higher Doppler factors than most blazars. This scenario can be tested more thoroughly using more complete statistics on gamma-ray blazars observed by the GLAST mission.

5. Summary

We have obtained first-epoch VLBA 15 GHz linear polarization images of the first large complete AGN sample to be selected solely on the basis of compact (milliarcsecond-scale) flux density. This project, entitled MOJAVE (Monitoring of Jets in Active Galactic Nuclei with VLBA Experiments), is a complement to the VLBA 2 cm Survey of Kellermann et al. (2004). Of the 133 AGN that satisfy our selection criteria, 88% are flat-spectrum blazars having relativistic jets pointed nearly directly at us. The remainder consist of powerful, nearby radio galaxies or peaked-spectrum radio sources. The sample contains 22 weak-lined BL Lacertae objects, and 38 AGN previously detected in high-energy gamma-rays by EGRET. At least 94% of the sample members have a typical one-sided “core-jet” morphology, which consists of a compact, bright core component located at the extreme end of a more diffuse jet. The very small number of sources with visible counter-jets reflects a strong Doppler favoritism toward jets viewed end-on.

Core component properties: The cores typically have brightness temperatures exceeding 10^{11} K, and 37% are completely unresolved, with lower limit values ranging from $\sim 10^{12}$ to 10^{14} K. The unresolved cores are more likely to show good alignments between their electric polarization vectors and the direction of the inner jet, perhaps as a result of a strong transverse shock located near the base of the jet. The cores of BL Lacertae objects show a particularly strong tendency toward these alignments, and have higher polarization levels than the quasars. The majority of cores in the sample have fractional polarization levels below 5 %, but the electric vector alignments suggest that this is not because of Faraday effects. Faraday depolarization is likely present, however, in the radio galaxy cores in our sample, none of which were detected in polarized emission.

Jet properties: We confirm the earlier findings of Lister (2001) that the jets of BL Lacs are more polarized than quasars at a given distance from the core. We also find that the trend of increasing fractional polarization with distance down the jet in blazars found by Lister (2001) extends to projected distances of at least 100 parsecs downstream. This increase in magnetic field order is not accompanied by an increase in electric vector alignment as found at 43 GHz by Lister & Smith (2000), although we note that our observations have three times poorer spatial resolution and probe regions much further downstream. We find many jet regions to have extremely high fractional polarization (i 50%), which indicates highly ordered magnetic fields in optically thin plasma. The electric vectors of the polarized regions are well-aligned with the jet ridge line in the case of BL Lac objects, consistent with strong, transverse shocks. The electric vectors in quasar jets have a variety of orientations, however, indicating either a different polarization mechanism, or a tendency toward oblique shocks.

Our results imply that the magnetic field properties of parsec-scale jets are closely tied to the broad line region in blazars. BL Lac objects have been postulated to be the end-on versions of lower power FR-I type radio galaxies Urry & Padovani (1995), and in such jets shocks may form more easily, leading to different polarization structures than those found in high-power quasars.

Gamma-Ray Blazars: We have examined the properties of the 35 blazars in MOJAVE that have been identified as likely candidates to EGRET gamma-ray sources. The jet features in these sources are typically twice as luminous as those in non-EGRET source, and are more likely to be linearly polarized. Since these differences occur tens to hundreds of parsecs downstream of where the gamma-rays are thought to be produced, the most likely explanation is that gamma-ray AGN have slightly higher Doppler factors than typical blazars, in agreement with the conclusions of Kellermann et al. (2004).

The authors wish to acknowledge the contributions of the other members of the MOJAVE project team: Hugh and Margo Aller, Tigran Arshakian, Marshall Cohen, Matthias Kadler, Ken Kellermann, Yuri Kovalev, Andrei Lobanov, Eduardo Ros, Rene Vermeulen, and Tony Zensus.

This research was supported by NSF grant 0406923-AST and made use of the following resources:

The NASA/IPAC Extragalactic Database (NED), which is operated by the Jet Propulsion Laboratory, California Institute of Technology, under contract with the National Aeronautics and Space Administration.

The VizieR database of astronomical catalogs (Ochsenbein et al. 2000).

The University of Michigan Radio Astronomy Observatory, which is supported by the National Science Foundation and by funds from the University of Michigan.

RATAN-600 observations were partly supported by the Russian State Program “Astronomy” and the Russian Ministry of Education and Science, the NASA JURRISS Program grant W-19611, and the Russian Foundation for Basic Research grant 01-02-16812.

Table 1. The Complete MOJAVE Sample

IAU Name (1)	Alias (2)	R.A. (J2000) (3)	Dec. (J2000) (4)	z (5)	Opt. Class (6)	V (7)	Radio Spectrum (8)	S_{VLBI} (Jy) (9)	γ -ray ID (10)
0003–066	NRAO 005	00 06 13.8928	–06 23 35.3353	0.347	B	18.5	Flat	2.83	...
0007+106	III Zw 2	00 10 31.0058	+10 58 29.5041	0.0893	G	15.4	Flat	3.00*	...
0016+731		00 19 45.7864	+73 27 30.0174	1.781	Q	19.0	Flat	2.40*	...
0048–097		00 50 41.3173	–09 29 05.2102	...	B	17.4	Flat	2.70*	...
0059+581		01 02 45.7623	+58 24 11.1366	...	U	...	Flat	3.31	...
0106+013		01 08 38.7710	+01 35 00.3171	2.107	Q	18.4	Flat	2.97	...
0109+224		01 12 05.8247	+22 44 38.7861	...	B	15.7	Flat	1.65*	...
0119+115		01 21 41.5950	+11 49 50.4131	0.570	Q	19.7	Flat	2.00*	...
0133+476	DA 55	01 36 58.5948	+47 51 29.1000	0.859	Q	19.5	Flat	4.95	...
0202+149	4C +15.05	02 04 50.4139	+15 14 11.0434	0.405	Q ^c	21.0	Flat	2.29	Y
0202+319		02 05 04.9253	+32 12 30.0956	1.466	Q	17.4	Flat	2.27	...
0212+735		02 17 30.8133	+73 49 32.6217	2.367	Q	20.0	Flat	2.69	...
0215+015		02 17 48.9547	+01 44 49.6990	1.715	B ^a	16.1	Flat	3.40*	...
0224+671	4C +67.05	02 28 50.0514	+67 21 03.0292	...	U	...	Flat	2.60*	...
0234+285	CTD 20	02 37 52.4056	+28 48 08.9900	1.207	Q	19.3	Flat	4.04	P
0235+164		02 38 38.9301	+16 36 59.2747	0.940	B ^a	15.5	Flat	1.62	Y
0238–084	NGC 1052	02 41 04.7985	–08 15 20.7518	0.0049	G	12.3	Flat	2.48	...
0300+470	4C +47.08	03 03 35.2422	+47 16 16.2754	...	B	17.0	Flat	1.70*	...
0316+413	3C 84	03 19 48.1601	+41 30 42.1030	0.0176	G	12.5	Flat	10.64	...
0333+321	NRAO 140	03 36 30.1075	+32 18 29.3423	1.263	Q	17.5	Flat	2.25	...
0336–019	CTA 26	03 39 30.9377	–01 46 35.8039	0.852	Q	18.4	Flat	3.44	Y
0403–132		04 05 34.0034	–13 08 13.6910	0.571	Q	17.1	Flat	2.30*	...
0415+379	3C 111	04 18 21.2770	+38 01 35.9000	0.0491	G	18.1	Steep	5.98	...
0420–014		04 23 15.8007	–01 20 33.0653	0.915	Q	17.0	Flat	10.60	Y
0422+004		04 24 46.8420	+00 36 06.3298	...	B	17.0	Flat	1.78	...
0430+052	3C 120	04 33 11.0955	+05 21 15.6194	0.0330	G	15.1	Flat	4.41	...
0446+112		04 49 07.6711	+11 21 28.5966	...	Q ^b	20.0	Flat	2.25	P
0458–020		05 01 12.8098	–01 59 14.2562	2.291	Q	18.1	Flat	2.33	Y
0528+134		05 30 56.4167	+13 31 55.1495	2.070	Q	20.0	Flat	7.95	Y
0529+075		05 32 38.9985	+07 32 43.3458	...	U	...	Flat	1.63	...
0529+483		05 33 15.8657	+48 22 52.8078	1.162	Q	19.9	Flat	1.50*	P
0552+398	DA 193	05 55 30.8056	+39 48 49.1650	2.363	Q	18.3	Peaked	5.02	...
0605–085		06 07 59.6992	–08 34 49.9781	0.872	Q	17.6	Flat	2.80	...
0607–157		06 09 40.9495	–15 42 40.6726	0.324	Q	18.0	Flat	7.26	...
0642+449	OH 471	06 46 32.0259	+44 51 16.5901	3.408	Q	18.5	Peaked	4.31	...
0648–165		06 50 24.5818	–16 37 39.7250	...	U	...	Flat	2.68	...
0716+714		07 21 53.4484	+71 20 36.3633	...	B	15.5	Flat	2.58	Y
0727–115		07 30 19.1124	–11 41 12.6004	1.591	Q	20.3	Flat	5.31	...
0730+504		07 33 52.5205	+50 22 09.0620	0.720	Q	19.3	Flat	1.60*	...
0735+178		07 38 07.3937	+17 42 18.9982	...	B	16.2	Flat	1.64	Y
0736+017		07 39 18.0338	+01 37 04.6180	0.191	Q	16.5	Flat	2.58	...
0738+313	OI 363	07 41 10.7033	+31 12 00.2286	0.630	Q	16.1	Flat	2.87	...
0742+103		07 45 33.0595	+10 11 12.6924	2.624	Q	24.0	Peaked	1.50	...
0748+126		07 50 52.0457	+12 31 04.8281	0.889	Q	18.7	Flat	3.25	...
0754+100		07 57 06.6429	+09 56 34.8521	0.266	B	15.0	Flat	1.83	...
0804+499		08 08 39.6662	+49 50 36.5304	1.432	Q	18.3	Flat	3.60*	...
0805–077		08 08 15.5360	–07 51 09.8863	1.837	Q	19.8	Flat	2.00*	P
0808+019		08 11 26.7073	+01 46 52.2200	0.93	B	17.2	Flat	1.90*	...
0814+425		08 18 15.9996	+42 22 45.4149	...	B	18.2	Flat	2.60*	...
0823+033		08 25 50.3383	+03 09 24.5201	0.506	B	16.8	Flat	1.50*	...
0827+243		08 30 52.0861	+24 10 59.8204	0.941	Q	17.3	Flat	1.99	Y
0829+046		08 31 48.8769	+04 29 39.0853	0.180	B	16.4	Flat	4.20*	Y
0836+710		08 41 24.3652	+70 53 42.1730	2.218	Q	17.3	Flat	2.24	Y

Table 1—Continued

IAU Name (1)	Alias (2)	R.A. (J2000) (3)	Dec. (J2000) (4)	<i>z</i> (5)	Opt. Class (6)	<i>V</i> (7)	Radio Spectrum (8)	<i>S_{VLBI}</i> (Jy) (9)	γ -ray ID (10)
0851+202	OJ 287	08 54 48.8749	+20 06 30.6408	0.306	B	15.4	Flat	4.12	Y
0906+015	4C +01.24	09 09 10.0915	+01 21 35.6176	1.018	Q	17.8	Flat	2.73	...
0917+624		09 21 36.2310	+62 15 52.1803	1.446	Q	19.5	Flat	2.00*	...
0923+392	4C +39.25	09 27 03.0139	+39 02 20.8519	0.698	Q	17.9	Flat	12.68	...
0945+408		09 48 55.3381	+40 39 44.5871	1.252	Q	18.4	Flat	1.59	...
0955+476		09 58 19.6716	+47 25 07.8425	1.873	Q	18.7	Flat	1.75	...
1036+054		10 38 46.7798	+05 12 29.0853	...	U	...	Flat	2.66	...
1038+064		10 41 17.1625	+06 10 16.9237	1.265	Q	16.7	Flat	1.85	...
1045–188		10 48 06.6206	–19 09 35.7269	0.595	Q	18.2	Flat	2.30*	...
1055+018	4C +01.28	10 58 29.6052	+01 33 58.8237	0.888	Q	18.3	Flat	5.30	...
1124–186		11 27 04.3924	–18 57 17.4416	1.048	Q	18.7	Flat	2.82	...
1127–145		11 30 07.0525	–14 49 27.3881	1.187	Q	16.9	Flat	3.39	P
1150+812		11 53 12.4991	+80 58 29.1545	1.250	Q	19.4	Flat	1.51	...
1156+295	4C +29.45	11 59 31.8339	+29 14 43.8269	0.729	Q	14.4	Flat	2.36	P
1213–172		12 15 46.7517	–17 31 45.4028	...	U	...	Flat	2.56	...
1219+044		12 22 22.5496	+04 13 15.7763	0.965	Q	18.0	Flat	1.50*	...
1222+216		12 24 54.4583	+21 22 46.3886	0.435	Q	17.5	Flat	1.76	Y
1226+023	3C 273	12 29 06.6997	+02 03 08.5981	0.158	Q	12.9	Flat	41.40	Y
1228+126	M87	12 30 49.4233	+12 23 28.0439	0.0044	G	12.9	Steep	2.97	...
1253–055	3C 279	12 56 11.1665	–05 47 21.5245	0.538	Q	17.8	Flat	24.89	Y
1308+326		13 10 28.6638	+32 20 43.7829	0.997	Q	15.2	Flat	3.98	...
1324+224		13 27 00.8613	+22 10 50.1630	1.400	Q	18.9	Flat	1.50*	P
1334–127		13 37 39.7827	–12 57 24.6932	0.539	Q	19.0	Flat	8.87	Y
1413+135		14 15 58.8174	+13 20 23.7126	0.247	B	20.5	Flat	1.72	...
1417+385		14 19 46.6137	+38 21 48.4752	1.832	Q	19.3	Flat	1.70*	P
1458+718	3C 309.1	14 59 07.5838	+71 40 19.8677	0.904	Q	16.8	Steep	1.50	...
1502+106	4C +10.39	15 04 24.9797	+10 29 39.1986	1.833	Q	18.6	Flat	1.95	...
1504–167		15 07 04.7869	–16 52 30.2673	0.876	Q	18.5	Flat	2.03	P
1510–089		15 12 50.5329	–09 05 59.8295	0.360	Q	16.5	Flat	2.93	Y
1538+149	4C +14.60	15 40 49.4915	+14 47 45.8848	0.605	B ^a	17.3	Flat	2.20*	...
1546+027		15 49 29.4368	+02 37 01.1634	0.412	Q	17.8	Flat	2.83	...
1548+056	4C +05.64	15 50 35.2692	+05 27 10.4482	1.422	Q	19.5	Flat	2.93	...
1606+106	4C +10.45	16 08 46.2031	+10 29 07.7758	1.226	Q	18.7	Flat	1.93	Y
1611+343	DA 406	16 13 41.0642	+34 12 47.9090	1.401	Q	18.1	Flat	4.52	Y
1633+382	4C +38.41	16 35 15.4929	+38 08 04.5006	1.807	Q	17.7	Flat	4.29	Y
1637+574		16 38 13.4562	+57 20 23.9791	0.751	Q	16.9	Flat	1.88	...
1638+398	NRAO 512	16 40 29.6327	+39 46 46.0285	1.666	Q	19.4	Flat	1.61	...
1641+399	3C 345	16 42 58.8099	+39 48 36.9939	0.594	Q	16.0	Flat	8.73	...
1655+077		16 58 09.0114	+07 41 27.5407	0.621	Q	20.0	Flat	2.09	...
1726+455		17 27 27.6508	+45 30 39.7313	0.714	Q	18.1	Flat	2.18	...
1730–130	NRAO 530	17 33 02.7057	–13 04 49.5482	0.902	Q	19.5	Flat	10.97	Y
1739+522	4C +51.37	17 40 36.9778	+52 11 43.4075	1.379	Q	18.7	Flat	1.77	Y
1741–038		17 43 58.8561	–03 50 04.6166	1.057	Q	20.4	Flat	7.01	Y
1749+096	4C +09.57	17 51 32.8185	+09 39 00.7285	0.320	B ^a	16.8	Flat	5.58	...
1751+288		17 53 42.4736	+28 48 04.9390	...	U	...	Flat	2.02	...
1758+388		18 00 24.7653	+38 48 30.6975	2.092	Q	18.0	Peaked	1.75	...
1800+440		18 01 32.3148	+44 04 21.9003	0.663	Q	17.9	Flat	1.50	...
1803+784		18 00 45.6839	+78 28 04.0185	0.680	B ^a	15.9	Flat	2.54	...
1823+568	4C +56.27	18 24 07.0683	+56 51 01.4908	0.663	B ^a	19.3	Flat	2.31	...
1828+487	3C 380	18 29 31.7388	+48 44 46.9710	0.692	Q	16.8	Steep	2.01	...
1849+670		18 49 16.0723	+67 05 41.6799	0.657	Q	16.9	Flat	1.74	...
1928+738	4C +73.18	19 27 48.4951	+73 58 01.5699	0.303	Q	16.1	Flat	3.93	...
1936–155		19 39 26.6577	–15 25 43.0583	1.657	Q	20.3	Flat	2.00*	P

Table 1—Continued

IAU Name (1)	Alias (2)	R.A. (J2000) (3)	Dec. (J2000) (4)	z (5)	Opt. Class (6)	V (7)	Radio Spectrum (8)	S_{VLBI} (Jy) (9)	γ -ray ID (10)
1957+405	Cygnus A	19 59 28.3566	+40 44 02.0965	0.0561	G	15.1	Steep	1.68	...
1958–179		20 00 57.0904	–17 48 57.6725	0.652	Q	18.6	Flat	2.67	...
2005+403		20 07 44.9448	+40 29 48.6041	1.736	Q	19.0	Flat	2.82	...
2008–159		20 11 15.7109	–15 46 40.2538	1.180	Q	18.3	Peaked	2.14	...
2021+317	4C +31.56	20 23 19.0173	+31 53 02.3059	...	U	...	Flat	2.16	...
2021+614		20 22 06.6816	+61 36 58.8047	0.227	G	19.0	Flat	2.73	...
2037+511	3C 418	20 38 37.0347	+51 19 12.6626	1.687	Q	21.0	Flat	2.33	...
2121+053		21 23 44.5173	+05 35 22.0932	1.941	Q	20.4	Flat	2.57	...
2128–123		21 31 35.2617	–12 07 04.7958	0.501	Q	16.1	Flat	3.17	...
2131–021	4C –02.81	21 34 10.3096	–01 53 17.2389	1.285	B ^a	19.0	Flat	2.21	...
2134+004		21 36 38.5863	+00 41 54.2133	1.932	Q	16.8	Peaked	6.34	...
2136+141	OX 161	21 39 01.3092	+14 23 35.9919	2.427	Q	18.9	Flat	2.75	...
2145+067	4C +06.69	21 48 05.4586	+06 57 38.6042	0.999	Q	16.5	Flat	10.37	...
2155–152		21 58 06.2819	–15 01 09.3280	0.672	Q	18.3	Flat	2.11	...
2200+420	BL Lac	22 02 43.2913	+42 16 39.9799	0.0686	B	14.7	Flat	5.67	Y
2201+171		22 03 26.8936	+17 25 48.2478	1.076	Q	19.5	Flat	2.01	...
2201+315	4C +31.63	22 03 14.9757	+31 45 38.2699	0.298	Q	15.6	Flat	3.28	...
2209+236		22 12 05.9663	+23 55 40.5438	1.125	Q	20.7	Flat	1.62	Y
2216–038		22 18 52.0377	–03 35 36.8794	0.901	Q	16.4	Flat	2.54	...
2223–052	3C 446	22 25 47.2592	–04 57 01.3907	1.404	Q	18.4	Flat	6.57	...
2227–088	PHL 5225	22 29 40.0843	–08 32 54.4354	1.562	Q	18.1	Flat	2.00	...
2230+114	CTA 102	22 32 36.4089	+11 43 50.9041	1.037	Q	17.3	Flat	4.86	P
2243–123		22 46 18.2319	–12 06 51.2773	0.630	Q	16.5	Flat	2.56	...
2251+158	3C 454.3	22 53 57.7479	+16 08 53.5608	0.859	Q	16.1	Flat	12.08	Y
2331+073		23 34 12.8281	+07 36 27.5520	...	U	...	Flat	1.50*	...
2345–167		23 48 02.6085	–16 31 12.0220	0.576	Q	18.4	Flat	2.54	...
2351+456	4C +45.51	23 54 21.6802	+45 53 04.2365	1.986	Q	20.6	Flat	1.80	P

Note. — Columns are as follows: (1) IAU Name (B1950.0); (2) Other Name; (3) Right Ascension (J2000); (4) Declination (J2000); (5) Redshift from Véron-Cetty & Véron (2003) (the redshift of 0202+149 is from Stickel et al. 1996, that of 0727–115 is from Zensus et al. 2002, that of 0742+103 is from Best et al. 2003, that of 0754+100 is from Carangelo et al. 2003, that of 0808+019 is from Jackson et al. 2002, and that of 2209+236 is from Sowards-Emmerd et al. 2003); (6) Optical classification according to the Véron-Cetty & Véron (2003) catalog, where Q = quasar, B = BL Lac object, G = active galaxy, and U = unidentified; (7) Optical V magnitude from Véron-Cetty & Véron (2003) catalog; (8) Description of radio spectrum from Kellermann et al. (2004); (9) Maximum 2 cm total cleaned VLBA flux density at any epoch during 1994–2003. Values with asterisks are inferred from single-dish observations (see §2.1); (10) EGRET gamma-ray source identification according to Mattox et al. (2001), Sowards-Emmerd et al. (2003) and Sowards-Emmerd et al. (2004), where Y = highly probable identification, P = probable identification.

^aSource classified as a quasar in the Véron-Cetty & Véron (2003) catalog.

^bSource classified as a possible BL Lac object in the Véron-Cetty & Véron (2003) catalog.

^cSource classified as a galaxy in the Véron-Cetty & Véron (2003) catalog.

Table 2. Optical and EGRET Gamma-Ray Classifications of the MOJAVE Sample

	Quasars	BL Lac Objects	Radio Galaxies	Unidentified	Total
EGRET	20	6	0	0	26
Probable EGRET	12	0	0	0	12
Non-EGRET	62	16	8	9	95
Total	94	22	8	9	133

Table 3. Summary of 15 GHz Image Parameters

Source (1)	Epoch (2)	B _{maj} (3)	B _{min} (4)	B _{pa} (5)	I _{tot} (6)	I _{peak} (7)	P _{tot} (8)	EVPA _{tot} (9)	I _{base} (10)	P _{base} (11)	Scale (12)
0003–066	2003 Feb 6	1.32	0.54	–5	2.83	1.83	101	17	1.7	1.7	4.9
0007+106	2004 Apr 10	1.16	0.51	–6	1.38	1.35	2	10	0.8	0.7	1.7
0016+731	2003 Aug 28	0.74	0.64	–87	1.07	1.01	9	108	0.7	1.7	8.4
0048–097	2003 Aug 28	1.30	0.49	–8	0.74	0.70	30	28	0.8	1.2	...
0059+581	2002 Nov 23	0.78	0.62	–9	3.30	3.16	63	11	1.1	1.2	...
0106+013	2003 Mar 29	1.20	0.51	–5	2.86	2.13	35	178	0.8	2.3	8.3
0109+224	2002 Jun 15	1.05	0.56	–6	1.01	0.93	43	86	0.5	0.9	...
0119+115	2003 Mar 1	0.96	0.47	–2	1.25	0.87	38	179	0.8	1.1	6.5
0133+476	2002 Jun 15	0.87	0.56	–2	4.48	4.20	140	115	1.8	1.9	7.7
0202+149	2002 Oct 9	1.28	0.60	–16	1.60	1.23	1	84	0.9	0.9	5.4
0202+319	2003 Mar 29	0.96	0.54	–6	2.27	2.10	36	103	1.2	1.3	8.5
0212+735	2003 May 9	0.74	0.66	–54	2.43	1.25	192	139	0.7	1.5	8.2
0215+015	2002 Jun 15	1.36	0.54	–10	0.90	0.75	14	93	0.7	0.8	8.5
0224+671	2002 Nov 23	0.77	0.65	36	1.30	0.68	6	126	0.7	0.8	...
0234+285	2002 Nov 23	1.08	0.55	–15	4.04	3.42	12	169	1.5	1.6	8.3
0235+164	2003 Mar 1	0.90	0.52	–3	1.62	1.45	72	167	0.8	1.1	7.9
0238–084	2002 Oct 9	3.14	1.79	9	0.62	0.34	< 2	...	1.9	1.9	0.1
0300+470	2002 Nov 23	0.81	0.61	–23	1.29	1.04	12	79	0.6	0.8	...
0316+413	2003 Mar 1	0.69	0.55	2	10.64	2.65	45	136	10.0	5.0	0.4
0333+321	2003 Mar 29	0.95	0.51	–12	2.25	1.73	44	48	0.7	2.0	8.4
0336–019	2003 Feb 6	1.32	0.56	–7	3.45	2.72	121	82	1.2	1.9	7.7
0403–132	2002 Jun 15	1.44	0.53	–8	1.40	1.32	7	21	0.7	1.1	6.5
0415+379	2002 Oct 9	1.44	0.79	3	1.66	1.17	9	98	2.0	1.2	1.0
0420–014	2003 Mar 1	1.14	0.46	–7	10.60	9.46	92	89	5.5	2.8	7.8
0422+004	2002 Jun 15	1.28	0.52	–7	1.78	1.64	137	5	0.8	1.0	...
0430+052	2003 Feb 6	1.20	0.56	–5	2.50	1.04	74	170	1.5	1.5	0.7
0446+112	2002 Jun 15	1.22	0.56	–8	2.25	2.11	22	166	2.5	1.5	...
0458–020	2003 Mar 1	1.12	0.45	–6	1.14	1.04	13	125	0.8	0.8	8.2
0528+134	2003 Feb 6	1.11	0.56	–6	3.17	2.64	137	123	1.2	0.9	8.3
0529+075	2002 Jun 15	1.30	0.58	–9	1.36	0.69	3	49	0.7	1.2	...
0529+483	2002 Oct 9	0.88	0.60	–16	1.03	0.90	16	155	0.6	0.8	8.3
0552+398	2003 Mar 29	0.91	0.52	–5	3.67	2.39	56	105	0.7	1.7	8.2
0605–085	2003 Feb 6	1.38	0.53	–6	1.50	1.00	26	145	0.7	1.0	7.7
0607–157	2003 Mar 1	1.24	0.46	–5	4.77	4.04	159	101	2.0	1.5	4.7
0642+449	2003 Mar 29	0.89	0.56	–10	4.31	3.45	136	32	0.7	2.0	7.4
0648–165	2002 Nov 23	1.44	0.51	–9	2.68	2.31	27	76	0.9	1.2	...
0716+714	2003 Aug 28	0.73	0.69	37	2.59	2.52	130	40	0.8	1.2	...
0727–115	2003 Mar 1	1.24	0.46	–6	5.31	4.09	165	97	1.3	2.1	8.5
0730+504	2002 Jun 15	0.79	0.58	4	0.86	0.72	6	97	0.5	0.8	7.2
0735+178	2002 Nov 23	1.19	0.57	–8	1.41	0.85	19	117	0.6	0.8	...
0736+017	2003 Mar 1	1.14	0.47	–8	1.79	1.49	6	141	0.9	1.3	3.2
0738+313	2003 Feb 6	1.10	0.71	–32	1.38	0.51	14	61	0.9	1.1	6.8
0742+103	2004 Apr 10	1.43	0.57	–14	1.32	0.59	3	136	0.8	1.0	8.0
0748+126	2003 Feb 6	1.15	0.59	–11	2.13	1.79	69	0	0.7	0.9	7.8
0754+100	2002 Nov 23	1.26	0.56	–7	1.83	1.38	101	20	0.6	0.7	4.1
0804+499	2004 Apr 10	0.77	0.58	–21	0.68	0.61	2	42	0.7	1.0	8.4
0805–077	2002 Jun 15	1.29	0.50	–7	1.58	1.28	8	40	0.9	1.1	8.4
0808+019	2004 Apr 10	1.32	0.52	–8	0.49	0.46	43	179	0.8	1.0	7.9
0814+425	2004 Apr 10	0.83	0.58	–20	0.77	0.67	16	79	0.7	0.9	...
0823+033	2003 Jun 15	1.23	0.52	–7	1.12	0.97	8	20	0.7	1.1	6.1
0827+243	2002 Jun 15	1.03	0.59	–15	1.99	1.77	13	66	0.7	2.5	7.9
0829+046	2003 Aug 28	1.31	0.59	–7	0.81	0.43	60	48	1.0	1.3	3.0
0836+710	2003 Mar 29	0.85	0.54	12	1.99	1.19	43	95	0.8	1.4	8.3
0851+202	2002 Oct 9	1.17	0.57	–12	4.12	3.48	97	14	1.3	1.5	4.5

Table 3—Continued

Source (1)	Epoch (2)	B _{maj} (3)	B _{min} (4)	B _{pa} (5)	I _{tot} (6)	I _{peak} (7)	P _{tot} (8)	EVPA _{tot} (9)	I _{base} (10)	P _{base} (11)	Scale (12)
0906+015	2003 Mar 29	1.20	0.52	-2	2.43	1.89	110	145	1.2	1.2	8.0
0917+624	2002 Jun 15	0.79	0.63	-79	0.90	0.57	33	32	0.7	1.1	8.4
0923+392	2002 Oct 9	0.91	0.61	-9	8.08	4.31	60	85	3.0	3.5	7.1
0945+408	2002 Oct 9	0.90	0.62	-9	1.59	1.00	7	56	0.6	0.8	8.3
0955+476	2002 Jun 15	0.74	0.60	-49	1.75	1.56	12	156	1.4	1.2	8.4
1036+054	2002 Jun 15	1.27	0.55	-10	2.66	2.55	37	74	0.9	1.5	...
1038+064	2002 Jun 15	1.28	0.54	-10	1.49	1.03	7	100	0.7	0.9	8.4
1045-188	2002 Jun 15	1.34	0.49	-7	1.33	1.11	50	64	1.0	1.2	6.7
1055+018	2003 Feb 6	1.28	0.53	-7	3.72	3.15	121	145	2.0	1.5	7.8
1124-186	2003 Mar 1	1.21	0.44	-4	1.41	1.30	27	23	0.9	1.1	8.1
1127-145	2002 Oct 9	1.55	0.52	-8	2.56	1.07	121	140	2.0	2.0	8.3
1150+812	2002 Jun 15	0.69	0.56	-78	1.51	0.98	30	32	0.8	1.2	8.3
1156+295	2002 Nov 23	0.99	0.57	-14	2.12	1.86	41	145	0.7	0.9	7.3
1213-172	2002 Jun 15	1.27	0.46	-7	1.68	1.11	50	171	0.7	1.2	...
1219+044	2002 Jun 15	1.20	0.49	-9	0.94	0.91	2	4	0.8	1.1	7.9
1222+216	2002 Jun 15	1.08	0.57	-12	0.82	0.56	51	158	0.7	0.9	5.6
1226+023	2002 Oct 9	1.66	0.55	-14	22.78	8.91	345	146	16.0	18.0	2.7
1228+126	2003 Feb 6	1.23	0.55	-9	2.74	1.28	5	135	0.7	1.0	0.1
1253-055	2002 Nov 23	1.44	0.52	-9	16.37	10.31	1244	52	5.0	7.0	6.3
1308+326	2003 Mar 29	0.93	0.56	1	2.99	2.48	87	119	0.7	1.5	8.0
1324+224	2002 Oct 9	1.26	0.58	-15	0.62	0.55	8	128	0.4	0.9	8.4
1334-127	2003 Mar 1	1.21	0.45	-5	5.05	4.31	78	165	2.0	3.0	6.3
1413+135	2002 Nov 23	1.21	0.58	-12	1.03	0.88	1	107	0.6	0.9	3.9
1417+385	2002 Jun 15	0.90	0.51	-21	0.90	0.84	19	148	0.8	1.0	8.4
1458+718	2003 Aug 28	0.81	0.64	-26	1.29	0.57	51	74	0.9	1.4	7.8
1502+106	2003 Mar 29	1.14	0.54	0	1.95	1.45	15	109	1.3	1.2	8.4
1504-167	2003 Feb 6	1.40	0.52	-5	1.60	0.93	18	68	1.7	1.3	7.7
1510-089	2002 Nov 23	1.50	0.51	-10	2.93	2.73	106	27	1.6	1.1	5.0
1538+149	2004 Apr 10	1.56	0.55	-19	1.18	0.97	129	140	0.7	1.0	6.7
1546+027	2003 Mar 29	1.20	0.51	-2	1.70	1.42	31	46	1.0	1.0	5.5
1548+056	2003 Mar 1	1.07	0.49	-5	2.93	1.66	88	100	1.0	1.5	8.4
1606+106	2002 Nov 23	1.25	0.59	-13	1.88	1.48	32	125	1.1	1.0	8.3
1611+343	2003 Feb 6	0.96	0.54	-9	4.07	2.72	96	15	1.0	1.1	8.4
1633+382	2003 Mar 29	0.95	0.54	4	4.29	3.48	47	156	0.7	1.0	8.4
1637+574	2002 Jun 15	0.78	0.62	-8	1.88	1.65	35	127	0.6	0.7	7.3
1638+398	2003 Mar 1	0.78	0.50	-6	0.88	0.68	51	168	0.8	1.0	8.5
1641+399	2002 Nov 23	0.86	0.60	-16	7.25	2.95	151	129	0.9	1.6	6.7
1655+077	2002 Oct 9	1.37	0.54	-9	1.09	0.86	36	130	0.9	1.6	6.8
1726+455	2002 Jun 15	0.82	0.66	-7	2.18	2.07	81	148	0.7	0.9	7.2
1730-130	2002 Oct 9	1.51	0.54	-7	5.66	4.75	30	71	2.2	5.3	7.8
1739+522	2003 Mar 29	0.87	0.57	18	1.40	1.30	36	166	1.1	1.1	8.4
1741-038	2003 Mar 1	1.17	0.47	-6	7.01	5.95	41	119	4.0	2.6	8.1
1749+096	2002 Jun 15	1.27	0.56	-11	3.42	3.13	67	177	1.9	1.2	4.7
1751+288	2002 Jun 15	1.01	0.49	-13	1.88	1.84	13	156	0.7	1.0	...
1758+388	2003 May 9	0.87	0.60	-11	1.38	1.26	21	33	0.6	0.8	8.3
1800+440	2003 Mar 29	0.89	0.51	14	1.21	1.10	11	53	0.6	1.2	7.0
1803+784	2003 Feb 6	0.67	0.65	47	1.92	1.33	83	100	0.7	0.9	7.1
1823+568	2003 May 9	0.75	0.62	-9	1.59	1.32	124	30	0.6	2.2	7.0
1828+487	2003 Mar 29	0.79	0.61	5	1.89	1.28	35	57	0.9	1.5	7.1
1849+670	2003 Jun 15	0.72	0.65	43	1.74	1.59	53	29	0.8	1.0	7.0
1928+738	2002 Jun 15	0.71	0.54	-58	3.93	2.47	34	79	0.9	1.7	4.5
1936-155	2002 Jun 15	1.49	0.52	-8	0.83	0.73	14	129	0.7	0.7	8.5
1957+405	2002 Nov 23	0.98	0.62	-38	1.53	0.64	3	146	1.1	1.1	1.1
1958-179	2002 Jun 15	1.50	0.52	-8	1.06	0.95	8	84	0.7	0.9	6.9

Table 3—Continued

Source (1)	Epoch (2)	B _{maj} (3)	B _{min} (4)	B _{pa} (5)	I _{tot} (6)	I _{peak} (7)	P _{tot} (8)	EVPA _{tot} (9)	I _{base} (10)	P _{base} (11)	Scale (12)
2005+403	2003 Mar 1	0.77	0.52	1	2.82	1.56	67	134	0.9	1.1	8.5
2008–159	2003 Jun 15	1.52	0.53	–7	2.14	1.96	3	128	0.8	1.0	8.3
2021+317	2003 Feb 6	1.07	0.58	–5	0.60	0.39	13	39	0.6	1.1	...
2021+614	2003 Mar 1	0.62	0.55	–8	2.26	0.99	< 1	...	0.9	1.1	3.6
2037+511	2002 Oct 9	0.82	0.62	–11	2.33	1.62	31	75	0.7	1.4	8.5
2121+053	2003 Mar 29	1.16	0.52	–4	2.57	2.13	138	1	1.0	1.7	8.4
2128–123	2003 May 9	1.39	0.51	–6	3.17	1.78	64	113	2.0	4.0	6.1
2131–021	2003 May 9	1.35	0.54	–8	2.21	1.14	52	92	1.0	1.0	8.4
2134+004	2002 Jun 15	1.37	0.53	–10	6.14	1.62	179	15	3.2	1.9	8.4
2136+141	2002 Nov 23	1.25	0.55	–16	2.75	2.15	89	127	1.0	0.9	8.1
2145+067	2003 Mar 1	1.01	0.44	–4	8.89	5.86	184	35	1.8	2.3	8.0
2155–152	2003 Mar 29	1.21	0.48	–4	2.11	1.27	71	57	2.5	3.0	7.0
2200+420	2002 Jun 15	0.84	0.55	–17	2.16	1.25	176	27	0.8	1.3	1.3
2201+171	2003 Jun 15	1.07	0.56	–6	2.01	1.83	35	170	0.7	1.0	8.1
2201+315	2002 Nov 23	1.04	0.55	–12	3.07	2.23	55	45	1.2	0.9	4.4
2209+236	2003 Mar 1	0.88	0.48	–1	0.85	0.62	81	35	0.8	1.1	8.2
2216–038	2002 Jun 15	1.41	0.54	–9	2.54	1.95	41	112	1.2	0.9	7.8
2223–052	2002 Oct 9	1.56	0.57	–10	5.17	3.72	158	149	2.6	2.2	8.4
2227–088	2003 Mar 29	1.28	0.50	–4	2.00	1.88	9	30	0.9	1.4	8.5
2230+114	2002 Oct 9	1.31	0.61	–13	3.54	2.32	42	91	2.0	2.4	8.1
2243–123	2002 Oct 9	1.60	0.56	–10	1.70	1.03	19	5	1.6	1.0	6.8
2251+158	2003 Mar 29	1.06	0.53	–9	9.64	3.24	127	178	2.7	6.5	7.7
2331+073	2002 Jun 15	1.21	0.51	–9	1.24	0.96	45	142	0.8	1.0	...
2345–167	2002 Oct 9	1.74	0.57	–10	1.91	1.39	10	67	0.7	1.0	6.6
2351+456	2002 Jun 15	0.87	0.57	–16	1.80	1.39	38	27	0.8	1.4	8.4

Note. — Columns are as follows: (1) IAU Name (B1950.0); (2) Date of VLBA observation; (3) FWHM major axis of restoring beam (milliarcseconds); (4) FWHM minor axis of restoring beam (milliarcseconds); (5) Position angle of major axis of restoring beam; (6) Total I flux density (Jy); (7) Peak flux density in the image (Jy per beam); (8) Total linearly polarized flux density (mJy); (9) Integrated electric vector position angle (deg.); (10) Lowest I contour in image (mJy per beam) (11) Lowest P contour in image (mJy per beam). (12) Linear scale in parsecs per milliarcsec.

Table 4. Core Component and Integrated Jet Properties

Source (1)	r (2)	P.A. (3)	I_c (4)	Maj. (5)	Ratio (6)	P.A. (7)	$T_{b,c}$ (8)	m_c (9)	EVPA _c (10)	m_{jet} (11)
0003-066	2.47	0.93	0.26	1	10.8	4.3	195	3.5
0007+106	0.94	> 12.9	< 0.06	...	< 14.6
0016+731	1.03	0.13	0.60	289	11.7	1.0	112	< 7.4
0048-097	0.73	0.21	0.34	12	11.4	4.2	209	< 17.0
0059+581	3.25	0.13	0.85	8	12.1	2.0	191	< 5.9
0106+013	1.84	0.28	0.39	3	11.5	1.5	185	2.4
0109+224	0.86	> 12.9	4.6	87	4.8
0119+115	0.90	0.30	0.13	26	11.6	5.6	0	5.9
0133+476	4.22	0.12	0.23	296	12.8	3.1	296	0.4
0202+149	0.55	156	0.18	> 12.0	< 0.1	...	< 2.6
0202+319	1.83	0.13	0.55	339	12.0	1.6	283	< 12.0
0212+735	0.74	296	0.74	0.44	0.32	294	10.8	5.5	140	7.3
0215+015	0.62	> 12.8	1.4	94	2.8
0224+671	0.16	6	0.76	0.41	0.23	9	11.0	1.1	280	1.4
0234+285	0.29	102	0.47	> 11.7	0.7	295	0.1
0235+164	1.34	0.22	0.40	3	11.6	4.8	347	< 9.9
0238-084	0.19	> 10.3	< 0.6	...	< 3.9
0300+470	1.04	0.19	0.24	303	11.8	1.0	85	0.7
0316+413	0.13	36	3.63	0.66	0.32	12	11.1	< 0.2	...	0.7
0333+321	1.88	0.28	0.31	308	11.6	0.5	75	2.3
0336-019	2.85	0.27	0.58	69	11.6	4.3	80	3.6
0403-132	1.14	> 13.5	0.6	206	< 9.1
0415+379	0.17	241	0.65	> 11.7	< 0.1	...	2.3
0420-014	7.86	> 14.1	0.9	104	0.4
0422+004	1.42	> 13.4	8.0	7	3.4
0430+052	1.13	0.26	1.00	...	10.9	< 0.2	...	4.5
0446+112	1.59	> 12.7	1.1	168	< 3.9
0458-020	1.08	0.12	0.80	74	11.7	1.3	313	1.1
0528+134	2.94	0.31	0.47	43	11.5	4.5	123	3.5
0529+075	1.06	0.69	0.81	342	10.1	0.4	340	1.0
0529+483	0.75	0.10	0.42	29	12.0	1.9	156	< 11.8
0552+398	2.38	0.30	0.80	42	11.2	1.6	285	2.1
0605-085	0.13	313	0.57	> 12.2	2.2	146	0.5
0607-157	4.57	0.25	0.33	278	12.1	3.6	103	1.9
0642+449	2.92	0.21	0.36	274	12.0	2.6	24	2.9
0648-165	2.36	0.22	0.08	49	12.5	1.0	255	< 4.2
0716+714	2.29	> 13.7	4.8	40	< 13.2
0727-115	2.54	> 13.8	3.1	275	2.3
0730+504	0.69	> 13.0	0.6	233	2.2
0735+178	0.10	261	0.57	> 12.8	3.0	98	5.6
0736+017	0.97	> 12.5	0.9	324	0.3
0738+313	3.74	356	0.31	> 11.4	< 0.3	...	1.2
0742+103	0.85	150	0.22	> 11.3	< 0.3	...	< 1.4
0748+126	1.81	0.15	0.51	45	11.9	3.4	176	2.1
0754+100	1.15	> 13.7	6.1	17	6.7
0804+499	0.62	0.12	0.54	29	11.6	0.6	188	0.8
0805-077	1.34	0.26	0.40	330	11.4	0.7	241	2.5
0808+019	0.44	> 12.4	8.7	179	< 12.4
0814+425	0.68	0.10	0.76	285	11.7	1.8	75	3.5
0823+033	0.87	> 12.3	1.1	27	0.6
0827+243	1.77	0.15	0.35	311	12.1	< 0.2	...	6.2
0829+046	0.43	0.23	0.33	61	11.1	4.7	52	4.8
0836+710	1.07	0.13	0.53	26	11.8	0.6	247	4.8
0851+202	3.41	> 13.5	1.6	200	6.8

Table 4—Continued

Source (1)	r (2)	P.A. (3)	I_c (4)	Maj. (5)	Ratio (6)	P.A. (7)	$T_{b,c}$ (8)	m_c (9)	EVPA _c (10)	m_{jet} (11)
0906+015	2.03	0.30	0.32	34	11.6	5.6	145	2.2
0917+624	0.30	121	0.15	> 11.4	3.4	198	1.9
0923+392	2.77	280	0.17	> 10.6	< 1.9	...	0.8
0945+408	0.93	> 13.1	1.8	107	2.0
0955+476	1.73	0.28	0.58	284	11.3	0.9	151	< 8.8
1036+054	2.62	0.22	0.40	344	11.8	1.4	255	< 6.3
1038+064	0.99	0.22	0.21	342	11.7	0.6	79	2.6
1045–188	0.10	329	0.81	> 12.8	3.1	70	5.3
1055+018	2.03	> 12.9	3.7	334	4.6
1124–186	1.27	0.11	0.18	322	12.5	1.9	198	0.3
1127–145	1.18	0.37	0.64	47	10.8	4.9	128	2.4
1150+812	1.02	0.19	0.29	52	11.7	0.7	197	3.7
1156+295	1.21	> 13.7	2.4	144	0.3
1213–172	0.40	287	0.34	> 11.8	1.9	137	3.8
1219+044	0.91	> 13.4	0.2	177	< 10.9
1222+216	0.51	> 12.7	4.1	347	11.7
1226+023	1.01	49	1.70	> 11.8	< 1.0	...	0.8
1228+126	0.98	0.37	0.38	334	11.0	< 0.08	...	< 2.5
1253–055	7.67	> 13.6	4.0	214	18.3
1308+326	2.56	0.19	0.41	331	12.0	3.3	296	5.0
1324+224	0.48	0.23	0.44	357	11.0	1.3	310	< 23.3
1334–127	3.76	0.23	0.11	354	12.5	1.5	200	5.5
1413+135	0.87	0.10	0.46	63	12.0	< 0.1	...	< 8.4
1417+385	0.84	0.08	0.44	83	12.2	2.0	152	2.6
1458+718	0.64	0.43	0.15	352	11.1	1.5	98	3.0
1502+106	0.12	289	0.73	> 12.4	0.8	109	2.0
1504–167	0.78	> 11.8	1.8	207	2.0
1510–089	0.19	168	0.82	> 12.2	3.7	205	< 2.5
1538+149	0.38	145	0.37	> 12.2	10.4	317	6.7
1546+027	1.46	0.32	0.17	2	11.6	1.8	223	1.4
1548+056	0.81	161	0.88	> 12.7	1.6	137	4.8
1606+106	0.94	0.20	0.25	38	11.7	2.5	311	3.7
1611+343	2.35	0.20	0.36	0	11.9	2.9	220	8.4
1633+382	3.47	0.12	0.57	12	12.4	1.6	336	2.7
1637+574	1.74	0.26	0.29	24	11.7	1.6	128	1.8
1638+398	0.69	0.28	0.55	331	10.9	7.0	169	< 6.3
1641+399	2.13	> 13.3	3.6	292	2.1
1655+077	0.68	> 12.3	3.2	314	0.7
1726+455	2.08	0.12	0.71	357	12.0	3.7	327	< 4.2
1730–130	4.81	0.19	0.24	10	12.5	0.3	163	3.2
1739+522	0.80	0.08	0.53	310	12.1	2.8	165	< 13.4
1741–038	6.13	0.17	0.61	70	12.2	0.6	119	3.7
1749+096	2.81	> 13.5	1.2	179	1.8
1751+288	1.86	0.08	0.84	33	12.2	0.7	154	< 20.3
1758+388	1.29	0.20	0.56	342	11.5	1.2	213	0.2
1800+440	1.06	0.13	0.20	22	12.2	1.3	222	< 24.5
1803+784	1.10	0.06	0.95	51	12.2	2.5	297	9.7
1823+568	1.26	0.15	0.30	17	12.0	8.1	210	0.4
1828+487	1.30	0.19	0.10	318	12.2	2.3	273	5.4
1849+670	1.59	0.19	0.21	351	12.0	3.3	208	< 11.9
1928+738	2.58	0.21	0.32	343	12.0	0.1	144	3.1
1936–155	0.74	0.14	0.44	288	11.6	1.6	133	0.8
1957+405	0.13	103	0.40	> 11.7	< 0.2	...	< 1.4
1958–179	0.93	0.13	0.52	281	11.7	0.5	287	< 4.6

Table 4—Continued

Source (1)	r (2)	P.A. (3)	I_c (4)	Maj. (5)	Ratio (6)	P.A. (7)	$T_{b,c}$ (8)	m_c (9)	EVPA _c (10)	m_{jet} (11)
2005+403	0.35	300	0.32	0.29	0.93	37	10.3	2.9	151	4.8
2008–159	2.07	0.32	0.28	19	11.6	< 0.05	...	< 5.1
2021+317	0.39	0.31	0.19	314	11.0	3.3	223	< 6.7
2021+614	3.16	34	0.04	> 9.8	< 3.7	...	< 0.3
2037+511	1.74	0.28	0.26	33	11.6	1.0	246	1.1
2121+053	2.18	0.18	0.47	13	11.9	6.5	182	0.4
2128–123	1.31	28	0.14	> 10.1	< 1.3	...	2.4
2131–021	0.80	> 11.7	4.1	87	2.9
2134+004	0.31	150	0.93	> 11.8	0.4	298	3.8
2136+141	0.11	130	1.47	0.20	0.33	337	11.8	2.7	309	3.2
2145+067	6.03	0.20	0.60	293	12.1	1.6	34	3.3
2155–152	1.40	0.29	0.36	34	11.4	3.6	224	6.5
2200+420	0.95	> 13.5	2.4	198	17.1
2201+171	1.77	0.12	0.24	54	12.4	1.9	173	2.1
2201+315	2.83	0.52	0.16	34	11.5	2.8	230	7.6
2209+236	0.79	0.45	0.12	46	11.2	10.0	39	14.6
2216–038	2.02	0.28	0.39	10	11.6	2.2	115	5.5
2223–052	0.15	317	2.07	> 12.5	3.3	142	3.9
2227–088	1.91	0.17	0.63	12	11.7	0.3	198	< 8.9
2230+114	2.39	0.22	0.39	314	11.8	1.7	128	3.8
2243–123	1.08	0.52	0.10	356	11.3	1.3	172	1.6
2251+158	3.46	0.21	0.89	283	11.6	1.1	305	1.0
2331+073	0.94	0.16	0.37	57	11.7	3.4	149	1.9
2345–167	1.65	0.52	0.24	311	11.1	0.8	90	2.3
2351+456	1.34	0.19	0.73	341	11.4	2.1	207	0.5

Note. — Columns are as follows: (1) IAU Name (B1950.0); (2) Core position offset from the map center; (3) Core position angle with respect to the map center; (4) Fitted Gaussian core flux density; (5) FWHM major axis of fitted core Gaussian (milliarcseconds); (6) Axial ratio of fitted core Gaussian; (7) Major axis position angle of fitted core Gaussian; (8) Log of core brightness temperature (K); (9) Fractional polarization at core position; (10) Electric vector position angle at core position; (11) Integrated fractional polarization of jet (per cent).

Table 5. Jet Component Properties

Source (1)	r (2)	P.A. (3)	Maj. (4)	Ratio (5)	P.A. (6)	I (7)	m (8)	EVPA (9)
0003–066	0.89	260	79	11.1	42
	1.96	304	58	18.8	16
	6.63	281	1.61	0.62	359	216	11.6	97
0007+106	0.09	274	439	< 0.06	...
0016+731	1.24	136	1.27	0.58	310	36	< 14.5	...
0048–097	1.25	359	9	4.7	208
0059+581	1.43	235	2.63	0.27	72	39	< 20.4	...
0106+013	0.30	235	506	2.6	201
	0.57	243	1.18	0.49	57	456	2.1	213
	2.96	239	2.54	0.45	9	48	< 30.3	...
0109+224	0.24	92	108	4.3	91
	1.94	87	2.44	0.26	85	38	13.4	230
0119+115	0.55	10	98	6.6	357
	1.65	359	0.57	0.61	347	181	7.0	281
	2.44	11	0.92	0.61	11	64	8.7	246
0133+476	0.57	331	0.91	0.25	335	194	2.4	300
	2.06	325	2.15	0.42	347	65	< 20.8	...
0202+149	0.62	338	0.35	0.20	330	1114	0.08	257
	0.77	320	110	< 0.1	...
	1.21	279	12	< 6.5	...
	3.16	297	1.81	0.69	279	59	< 6.1	...
	5.19	302	0.95	0.27	40	34	< 3.4	...
	5.35	317	2.50	0.52	44	91	< 5.2	...
	0.18	279	336	1.7	284
0202+319	0.37	337	60	1.7	106
	1.64	11	6	< 23.9	...
	7.57	353	4.35	0.28	325	33
	0.77	115	0.48	0.69	76	1560	10.8	136
0212+735	1.75	108	0.58	1.00	...	27	5.9	154
	3.15	105	1.22	0.57	305	43	< 10.5	...
	14.27	93	2.20	0.63	318	37	< 27.9	...
0215+015	0.20	105	0.54	0.62	310	200	1.2	94
	1.02	111	1.42	0.36	6	50	5.1	96
	3.16	105	3.21	0.48	350	28	< 17.2	...
0224+671	0.73	4	0.31	1.00	...	486	2.3	354
	7.75	354	3.83	0.55	6	53	< 20.5	...
0234+285	0.31	283	0.30	0.48	346	3401	0.7	7
	4.77	348	5.02	0.42	351	181	< 12.4	...
0235+164	0.20	253	0.45	0.43	300	253	4.9	167
	0.56	330	13	6.0	165
0238–084	0.52	79	0.87	1.00	...	167	< 0.6	...
	6.49	71	3.01	0.40	48	69	< 4.6	...
	12.06	62	12	< 28.2	...
	1.58	245	0.68	1.00	...	109	< 1.2	...
	3.80	247	2.70	0.13	71	80	< 3.7	...
	9.98	246	0.46	1.00	...	17	< 17.6	...
0300+470	17.33	246	6
	0.71	148	0.75	0.66	355	219	0.6	129
	2.19	139	2.29	0.74	318	30	< 22.4	...
0316+413	0.73	338	0.47	0.18	68	609	< 0.7	...
	8.93	350	2.90	0.68	360	516	< 22.4	...
	0.82	226	0.59	0.67	54	3485	< 0.2	...
	1.54	206	1.09	0.43	304	1526	< 0.7	...
	12.47	180	4.98	0.84	336	2255	< 15.2	...

Table 5—Continued

Source (1)	r (2)	P.A. (3)	Maj. (4)	Ratio (5)	P.A. (6)	I (7)	<i>m</i> (8)	EVPA (9)
0333+321	0.61	128	41	2.1	54
	1.44	123	0.96	0.41	319	112	8.5	48
	2.31	125	14	< 9.0	...
	3.61	124	0.94	0.65	41	40	< 12.3	...
	5.81	128	1.58	0.47	330	115	< 5.7	...
0336–019	8.56	126	8
	0.41	30	283	3.3	73
	1.37	55	1.24	0.58	295	236	4.0	97
0403–132	3.37	54	2.07	0.61	289	62	< 14.9	...
	0.29	179	0.17	1.00	...	216	0.5	218
	1.98	183	2.09	0.15	334	32	< 6.0	...
0415+379	9.90	162	5.82	0.39	338	18
	0.33	63	0.18	1.00	...	645	< 0.1	...
	1.05	62	0.54	1.00	...	134	< 0.5	...
	2.31	65	0.80	1.00	...	115	7.0	74
	4.57	62	0.95	1.00	...	56	4.1	121
0420–014	6.06	64	1.25	1.00	...	57	10.0	149
	0.20	237	0.41	0.46	22	2462	0.7	265
	1.16	197	1.70	0.45	26	255	4.7	228
	4.01	173	2.26	0.74	15	79	< 43.6	...
0422+004	0.40	4	0.30	0.67	331	300	8.2	5
	1.05	2	1.29	0.46	35	50	7.7	176
0430+052	0.63	245	0.48	1.00	...	316	0.5	137
	1.30	235	141	3.8	317
	1.78	242	156	2.0	175
	4.40	242	1.38	1.00	...	186	5.5	181
	6.95	240	0.96	0.35	73	341	9.5	5
	7.60	248	23	13.6	350
0446+112	10.79	251	4.64	0.44	275	219	< 10.6	...
	0.20	124	0.15	1.00	...	637	1.3	163
	0.96	108	0.77	1.00	...	20	< 7.8	...
0458–020	2.85	312	3.05	0.61	278	55	< 21.4	...
	5.08	306	1.12	0.51	13	17	< 11.0	...
0528+134
	1.40	40	1.43	0.41	20	153	5.8	311
	3.22	18	11	< 8.4	...
0529+075	4.34	25	1.92	0.67	12	42	< 8.8	...
	1.36	322	2.17	0.81	302	284	< 1.8	...
0529+483	0.32	34	0.25	0.85	273	258	0.8	335
	1.43	26	1.05	1.00	...	9	< 17.8	...
	4.03	25	4.53	0.56	39	18
0552+398	0.40	288	1.02	0.60	283	1270	1.1	112
0605–085	0.28	132	0.18	1.00	...	560	3.0	139
	1.25	123	0.84	0.72	28	168	1.2	37
	2.84	119	7	< 5.2	...
	4.23	116	2.93	0.65	275	173	< 5.6	...
0607–157	0.58	65	92	3.9	101
	2.70	77	2.37	0.76	46	96	< 14.1	...
0642+449	0.30	87	0.30	0.75	310	1362	3.8	35
0648–165	0.29	272	0.14	1.00	...	233	0.5	257
	1.06	281	0.98	0.61	296	66	< 4.1	...
	3.27	230	5
	9.30	240	4.57	0.66	49	20
0716+714	0.15	35	0.07	1.00	...	264	5.2	40
	0.67	34	0.30	1.00	...	15	6.9	41

Table 5—Continued

Source (1)	r (2)	P.A. (3)	Maj. (4)	Ratio (5)	P.A. (6)	I (7)	m (8)	EVPA (9)
	2.00	19	0.81	1.00	...	7	< 40.9	...
	3.53	12	2
0727-115	0.22	254	0.31	0.30	271	2428	3.1	274
	0.52	271	0.70	0.62	326	239	3.2	277
	2.14	300	3.36	0.38	324	66	< 30.4	...
	1.93	1	0.57	1.00	...	23	< 21.2	...
0730+504	0.58	224	0.74	0.28	25	109	0.9	279
	1.52	217	0.52	0.72	20	32	5.7	134
	3.26	213	1.32	0.91	281	21	< 19.0	...
	5.48	209	1.17	1.00	...	6
0735+178	0.21	84	287	3.5	95
	0.50	64	0.19	1.00	...	179	3.1	88
	1.04	59	0.60	1.00	...	218	2.2	2
	1.50	68	0.91	1.00	...	114	3.7	150
	3.09	61	1.39	1.00	...	30	10.8	174
0736+017	0.15	288	0.46	0.24	290	761	0.7	317
	3.39	289	4.68	0.11	294	47	< 20.4	...
	6.29	292	5	< 33.9	...
	12.13	275	5.05	0.63	296	47
0738+313	0.79	181	0.27	1.00	...	133	1.5	108
	1.37	184	0.50	1.00	...	135	2.5	245
	3.67	177	0.52	0.59	327	458	0.6	49
	4.02	171	0.41	1.00	...	211	1.4	107
	4.02	162	2.64	0.30	305	120	2.9	259
0742+103	0.85	329	0.35	1.00	...	588	< 0.2	...
	1.54	322	0.49	1.00	...	128	< 0.4	...
	2.49	351	1.16	1.00	...	348	< 0.8	...
0748+126	0.51	69	0.44	0.28	70	170	3.2	189
	2.36	113	2.09	0.40	301	127	< 2.8	...
	4.75	109	7	< 20.2	...
	6.16	107	4
0754+100	0.31	15	281	6.1	18
	1.36	13	0.34	0.92	360	327	3.6	22
	3.08	24	1.08	0.51	322	35	22.6	53
	4.38	15	3.28	0.46	338	38	25.4	214
0804+499	1.06	129	2.06	0.48	336	60	< 8.1	...
0805-077	1.60	341	0.38	0.61	88	125	6.1	348
	2.06	323	2.05	0.51	321	111	< 3.6	...
0808+019	0.57	183	0.10	1.00	...	40	10.4	178
	1.82	184	5	< 19.5	...
0814+425	1.33	91	0.76	0.73	52	74	5.1	98
	3.12	150	4	< 35.6	...
0823+033	0.38	23	0.24	1.00	...	167	0.7	24
	2.18	25	1.73	1.00	...	65	< 14.4	...
0827+243	0.30	127	53	0.3	155
	1.24	112	0.41	0.53	355	114	7.6	254
	1.43	129	1.09	0.72	321	28	5.6	260
	5.34	137	2.68	0.54	312	27
0829+046	0.53	67	158	14.2	49
	0.84	67	0.69	0.51	54	140	11.8	51
	2.95	69	2.79	0.31	63	81	< 7.8	...
0836+710	0.58	221	0.36	0.63	11	629	2.2	240
	1.30	227	0.43	0.31	9	66	6.9	270
	2.80	216	1.93	0.31	27	123	11.8	297

Table 5—Continued

Source (1)	r (2)	P.A. (3)	Maj. (4)	Ratio (5)	P.A. (6)	I (7)	m (8)	EVPA (9)
	7.57	219	4.23	0.39	33	32
	12.97	210	4.87	0.33	11	69	< 22.4	...
0851+202	0.40	237	0.29	1.00	...	207	1.6	182
	1.26	244	0.39	0.70	284	452	8.4	194
	1.94	243	20	3.0	199
	3.70	250	2.18	1.00	...	30
0906+015	0.57	51	205	3.5	328
	1.02	48	165	1.9	213
0917+624	0.28	298	346	3.6	27
	0.66	300	188	4.2	38
	0.85	319	0.32	1.00	...	120	4.5	41
	1.46	336	0.84	1.00	...	46	< 4.3	...
	3.11	350	5
	6.07	337	9	< 24.1	...
0923+392	0.65	88	0.48	1.00	...	150	< 3.2	...
	1.58	95	0.11	1.00	...	100	2.8	26
	2.69	100	0.76	0.72	71	6533	1.9	101
	2.97	101	1107	2.6	270
0945+408	0.31	130	92	1.2	119
	0.87	125	0.42	1.00	...	314	2.6	24
	1.16	115	0.54	0.68	41	163	3.1	47
	1.85	118	0.55	1.00	...	33	< 1.6	...
	9.76	115	5.25	0.42	279	67	< 43.3	...
0955+476	0.94	127	0.70	1.00	...	12	< 2.7	...
1036+054	1.82	351	0.69	1.00	...	22	< 6.5	...
1038+064	0.57	163	98	1.0	76
	1.82	156	0.41	0.91	314	350	2.9	159
	2.69	154	1.82	0.39	336	32	4.4	135
	6.96	146	1.76	0.38	316	12	< 23.8	...
1045-188	0.38	150	386	3.5	245
	0.83	155	0.20	1.00	...	83	4.7	238
	1.68	159	0.41	1.00	...	31	10.3	234
	7.18	146	1.26	0.40	318	17	< 18.5	...
1055+018	0.18	308	1249	3.6	331
	1.62	301	0.63	0.74	341	90	10.3	305
	4.59	309	6.64	0.32	313	306	12.2	305
	9.46	302	24	18.1	98
1124-186	0.62	169	0.89	0.71	347	131	1.9	19
1127-145	0.57	98	0.46	1.00	...	644	7.2	144
	1.31	84	0.80	1.00	...	114	< 2.7	...
	4.49	82	1.38	0.76	78	532	< 1.2	...
	6.19	74	2.41	0.39	4	93	< 9.1	...
1150+812	0.72	218	0.55	0.38	9	92	8.6	223
	1.16	193	0.83	0.18	275	29	5.5	228
	2.45	177	1.05	0.63	316	340	5.8	198
	3.95	162	3.58	0.32	332	36
1156+295	0.26	356	0.12	1.00	...	602	2.4	329
	0.45	16	0.44	0.58	15	258	1.9	333
	1.82	343	0.52	1.00	...	10	< 12.6	...
	4.05	3	1.77	0.35	275	11	< 33.2	...
	7.16	19	6.82	0.55	54	49
1213-172	0.43	104	0.30	0.29	88	1278	4.1	167
	2.17	131	0.82	1.00	...	40	< 7.0	...
1219+044	0.74	185	0.24	1.00	...	28	< 0.4	...

Table 5—Continued

Source (1)	r (2)	P.A. (3)	Maj. (4)	Ratio (5)	P.A. (6)	I (7)	m (8)	EVPA (9)
1222+216	0.34	357	0.15	1.00	...	67	4.4	348
	1.15	358	0.20	1.00	...	12	3.6	348
	2.90	352	1.09	0.41	342	112	18.4	328
	4.07	357	10	0.59	330	65	12.2	346
	5.27	3	0.94	1.00	...	25	18.0	336
	7.90	7	1.90	1.00	...	14	< 42.8	...
1226+023	12.87	352	2.38	0.42	30	19	< 23.2	...
	0.52	208	1585	0.6	261
	1.02	229	0.55	0.51	318	10860	4.2	218
	1.70	233	411	2.2	196
	3.06	238	1.07	1.00	...	1178	6.1	152
	3.90	227	0.34	1.00	...	1298	8.4	162
1228+126	4.83	227	0.58	1.00	...	1205	7.3	342
	10.00	243	1.26	0.59	14	3277	12.3	284
	14.33	238	3.16	0.40	42	1149	< 12.5	...
	0.18	262	0.95	0.38	284	769	< 0.09	...
	1.51	287	1.68	0.66	78	510	< 0.8	...
	3.51	280	2.46	0.50	66	149	< 3.6	...
1253-055	7.43	278	3.78	0.47	293	87	< 13.1	...
	0.33	215	3515	7.6	214
	1.30	232	1.84	0.09	57	3610	21.0	236
	3.02	237	1.14	0.41	3	725	41.8	258
1308+326	5.06	236	0.64	0.60	343	740	11.0	60
	0.46	291	86	2.5	277
	2.10	314	1.01	0.57	80	234	7.4	143
1324+224	0.32	330	0.41	0.53	40	118	1.4	307
	0.56	205	1.26	0.81	276	11	1.3	309
1334-127	0.50	166	0.29	0.52	341	1034	3.2	159
	1.69	142	0.78	0.49	320	209	8.8	119
	2.69	149	0.31	1.00	...	28	< 6.2	...
1413+135	0.43	247	0.18	1.00	...	91	< 0.3	...
	0.89	245	17	< 2.3	...
	2.17	247	0.98	1.00	...	18	< 14.3	...
	4.06	250	1.40	1.00	...	13	< 32.3	...
	7.50	250	1.78	1.00	...	13	< 37.0	...
1417+385	0.76	163	1.47	0.70	36	59	2.3	327
1458+718	0.94	157	0.53	0.39	5	291	5.5	95
	23.57	166	5.19	0.30	315	114	< 21.1	...
	24.22	163	1.36	0.68	17	120	4.4	84
	26.15	166	3.88	0.50	0	124	17.9	257
1502+106	0.20	109	834	1.3	102
	0.54	108	122	2.1	92
	1.07	121	95	< 1.0	...
	1.54	121	50	< 2.0	...
	2.19	120	28	6.3	151
	2.97	120	24	11.8	310
1504-167	0.40	205	252	1.4	210
	1.27	192	179	4.8	265
	2.40	189	65	< 2.0	...
1510-089	3.95	161	1.20	0.85	18	290	2.8	296
	0.26	348	0.05	1.00	...	1975	3.9	206
	0.83	302	0.26	1.00	...	43	1.6	49
	1.67	320	0.50	1.00	...	53	< 2.4	...
	2.52	318	9	< 7.5	...

Table 5—Continued

Source (1)	r (2)	P.A. (3)	Maj. (4)	Ratio (5)	P.A. (6)	I (7)	<i>m</i> (8)	EVPA (9)
1538+149	4.29	328	1.46	1.00	...	28	< 19.8	...
	0.53	325	0.40	0.16	321	746	11.8	319
	1.50	328	1.45	0.27	328	55	12.6	325
1546+027	3.26	318	4	< 29.9	...
	1.26	174	0.88	0.18	318	181	1.5	219
	2.75	174	1.11	1.00	...	55	< 4.4	...
1548+056	0.69	358	0.17	1.00	...	282	2.2	279
	0.90	342	0.11	1.00	...	1351	3.3	99
	1.12	1	0.48	1.00	...	354	4.0	86
1606+106	2.41	6	0.14	1.00	...	25	7.7	64
	4.51	4	1.89	1.00	...	28	< 39.4	...
	0.23	336	0.31	1.00	...	651	2.8	313
1611+343	0.49	288	0.25	1.00	...	130	2.6	308
	1.24	303	1.21	0.42	312	122	4.9	230
	2.38	320	1.30	1.00	...	28	< 5.4	...
1633+382	0.32	164	0.68	0.35	345	691	1.7	224
	1.28	158	0.56	0.72	356	158	6.8	136
	2.90	172	0.43	0.78	86	196	11.2	189
1637+574	3.79	170	3.24	0.52	82	678	15.2	350
	0.51	288	0.75	0.40	294	252	1.7	326
	1.86	269	1.11	0.55	64	139	1.8	37
1638+398	2.30	282	2.50	0.50	278	274	3.2	356
	3.11	267	0.76	0.58	342	144	11.6	65
	1.00	205	1.92	0.17	17	93	4.8	286
1641+399	3.80	200	1.16	0.65	27	31	< 6.2	...
	0.32	282	133	4.8	164
	0.52	216	28	3.7	173
1655+077	0.78	175	10	4.0	356
	0.25	275	1116	3.4	304
	1.04	271	0.55	0.43	283	1498	5.5	299
1726+455	1.55	271	0.79	0.92	283	1584	2.2	330
	2.50	264	1.01	0.37	291	532	3.8	233
	3.83	271	1.34	1.00	...	171	5.6	214
1730–130	7.14	290	3.15	1.00	...	161	< 17.1	...
	0.29	321	0.06	1.00	...	223	3.7	314
	0.81	322	55	4.3	314
1739+522	1.85	327	0.59	1.00	...	56	< 4.2	...
	8.68	314	2.45	0.64	69	76	< 24.6	...
	0.31	237	45	3.7	149
1741–038	0.81	237	5	3.8	157
	2.05	262	0.86	0.90	324	39	< 5.1	...
	1.77	31	0.76	0.51	32	317	6.2	240
1749+096	2.29	8	1.61	0.57	352	304	6.4	101
	6.95	14	3.06	0.61	41	211	< 27.6	...
	23.71	1	5.99	0.49	42	122
1751+288	0.15	31	0.24	0.68	30	571	2.7	347
	1.20	26	2.24	1.00	...	30	< 4.2	...
	0.50	219	266	0.6	122
1749+096	0.73	182	361	1.1	150
	0.74	155	155	1.1	139
	1.24	202	57	4.4	228
1751+288	0.49	6	0.16	1.00	...	555	2.9	354
	1.87	16	0.45	1.00	...	29	< 7.5	...
	1.26	24	2

Table 5—Continued

Source (1)	r (2)	P.A. (3)	Maj. (4)	Ratio (5)	P.A. (6)	I (7)	m (8)	EVPA (9)
1758+388	0.48	270	0.82	0.46	61	75	2.4	35
1800+440	0.44	202	0.42	0.74	8	114	0.7	232
	1.35	203	0.63	0.26	285	13	< 6.3	...
	5.05	200	5.15	0.08	29	10
1803+784	0.26	285	0.45	0.53	277	400	2.6	297
	1.40	272	0.34	0.79	340	255	15.0	272
	1.76	270	0.81	0.46	318	73	11.6	268
	2.94	267	2.10	0.29	298	20	< 16.6	...
	5.70	266	4.33	0.53	76	62	< 43.5	...
1823+568	0.43	199	0.10	1.00	...	241	10.4	204
	1.00	197	0.20	1.00	...	9	12.7	199
	1.83	198	0.54	0.38	3	54	< 5.7	...
	4.18	204	1.06	1.00	...	12
	6.10	200	0.33	1.00	...	5
	7.32	199	0.92	1.00	...	11
1828+487	1.12	318	1.51	0.15	328	257	5.9	262
	2.74	332	15	< 9.2	...
	4.98	330	1.07	0.58	56	45	< 7.7	...
	10.83	328	1.69	0.58	293	141	26.0	190
1849+670	0.29	324	0.28	0.65	82	104	2.9	23
	0.89	320	16	< 3.1	...
	3.20	314	5
	5.26	302	5	< 44.4	...
1928+738	0.89	156	0.62	0.27	336	774	1.2	245
	2.16	158	0.64	0.85	70	192	3.9	203
	3.42	164	0.77	0.61	26	144	8.2	90
	4.62	168	1.52	0.45	307	135	< 5.4	...
	12.44	168	2.45	0.58	21	70	< 34.9	...
1936-155	0.65	122	0.51	1.00	...	72	1.6	133
	1.19	129	12	2.4	128
	1.11	189	3.19	0.11	354	13	1.5	137
1957+405	0.68	283	1.02	0.39	277	790	< 0.2	...
	2.62	281	0.92	0.49	283	121	< 1.7	...
	6.07	282	0.80	1.00	...	21	< 14.2	...
	0.73	109	0.36	1.00	...	160	< 0.6	...
	2.91	108	14	< 14.7	...
1958-179	0.42	207	0.99	0.35	71	126	0.4	216
2005+403	0.36	120	0.40	0.72	25	1871	3.9	147
	0.80	85	22	2.4	148
	1.56	98	0.82	0.88	36	541	8.0	97
	1.24	155	13	2.9	149
2008-159	1.27	8	1.12	0.14	14	50	1.8	125
2021+317	0.65	168	0.58	0.53	40	112	1.7	217
	1.62	180	1.07	0.45	37	44	< 3.5	...
	3.67	162	2.14	0.45	313	17	< 32.2	...
2021+614	3.21	214	0.40	0.82	305	1283	< 0.1	...
	2.61	216	0.62	0.41	356	533	< 0.2	...
	0.99	220	0.63	1.00	...	38	< 6.8	...
	3.89	31	0.58	0.87	325	328	< 0.7	...
2037+511	1.23	219	1.71	0.46	72	156	< 4.2	...
	7.20	219	3.16	0.80	7	425	< 5.2	...
2121+053	0.73	276	0.44	0.43	80	261	2.0	303
	1.23	294	0.85	0.56	4	116	< 1.3	...
2128-123	0.33	216	316	< 0.8	...

Table 5—Continued

Source (1)	r (2)	P.A. (3)	Maj. (4)	Ratio (5)	P.A. (6)	I (7)	<i>m</i> (8)	EVPA (9)
	1.32	208	0.50	0.42	19	2084	1.7	123
	2.02	209	170	5.1	278
	5.26	212	1.37	0.46	20	457	5.0	112
2131-021	0.57	100	1.07	0.27	300	1316	2.7	98
	2.05	97	0.72	0.81	47	80	5.2	283
2134+004	0.51	332	0.39	1.00	...	1115	1.1	182
	0.99	286	0.62	1.00	...	1201	8.2	217
	1.84	292	296	2.9	342
	2.13	268	0.75	1.00	...	2573	4.9	19
2136+141	0.31	310	0.24	0.48	25	896	3.5	308
	0.55	287	231	4.6	304
	0.87	268	0.18	1.00	...	90	3.0	286
	1.07	247	0.49	1.00	...	46	5.0	257
	3.88	213	4.05	0.22	347	19	< 27.4	...
2145+067	0.61	122	0.62	0.44	316	2765	2.9	38
	1.40	118	54	< 1.9	...
2155-152	1.04	207	259	4.0	134
	3.13	211	2.60	0.39	31	451	19.0	63
2200+420	0.26	196	0.10	1.00	...	402	3.6	198
	1.18	194	0.25	1.00	...	69	14.7	201
	1.58	199	0.34	1.00	...	95	20.0	204
	2.33	199	0.63	1.00	...	397	23.9	210
	3.39	194	1.26	1.00	...	102	19.7	214
	5.06	182	2.58	1.00	...	143	20.3	201
2201+171	0.38	37	0.29	0.16	271	184	2.3	356
	1.48	51	0.74	0.63	51	31	7.3	124
	6.15	44	4.50	0.32	88	20
2201+315	1.82	209	0.56	1.00	...	64	19.3	165
	4.47	221	1.67	0.63	82	187	7.0	318
2209+236	1.31	32	0.50	0.67	69	74	17.6	191
2216-038	1.97	188	1.62	0.37	357	515	4.1	200
2223-052	0.30	135	0.24	1.00	...	2027	4.2	137
	0.73	84	0.82	0.35	21	895	3.6	176
	3.31	105	1.26	0.49	310	125	< 3.7	...
	6.14	94	2.07	1.00	...	31	< 35.2	...
2227-088	0.37	312	0.16	1.00	...	52	0.5	316
	1.41	336	1.92	0.45	356	33	< 6.6	...
2230+114	0.89	126	0.38	0.21	288	307	5.9	100
	1.72	145	0.43	1.00	...	132	8.2	106
	3.28	143	0.53	1.00	...	37	33.0	261
	5.73	159	3.35	0.30	328	387	12.4	211
	10.01	159	5.17	0.53	329	274	< 21.1	...
	17.04	143	4.01	0.71	288	94
2243-123	1.79	359	0.89	0.27	356	483	2.7	19
	3.63	21	1.11	0.99	342	118	< 2.3	...
	10.98	31	3.44	0.31	273	28
2251+158	0.78	269	0.43	0.80	59	4160	1.1	318
	1.64	254	1.78	0.34	321	630	7.8	214
	6.58	285	50	0.29	322	863	< 12.3	...
2331+073	0.43	239	259	4.8	317
	0.87	228	23	5.2	302
2345-167	1.67	131	0.55	1.00	...	87	5.0	196
	3.39	120	1.34	0.68	277	175	< 1.6	...
2351+456	0.34	327	0.35	1.00	...	202	3.2	204

REFERENCES

Aller, M. F., Aller, H. D., & Hughes, P. A. 2003, *ApJ*, 586, 33

Aloy, M., Martí, J., Gómez, J., Agudo, I., Müller, E., & Ibáñez, J. 2003, *ApJ*, 585, L109

Bennett, C. L., et al. 2003, *ApJS*, 148, 97

Best, P. N., Peacock, J. A., Brookes, M. H., Dowsett, R. E., Röttgering, H. J. A., Dunlop, J. S., & Lehnert, M. D. 2003, *MNRAS*, 346, 1021

Browne, I. W. A., et al. 2003, *MNRAS*, 341, 13

Cawthorne, T. V. & Cobb, W. K. 1990, *ApJ*, 350, 536

Cawthorne, T. V., & Wardle, J. F. C. 1988, *ApJ*, 332, 696

Cawthorne, T. V., Wardle, J. F. C., Roberts, D. H., & Gabuzda, D. C. 1993, *ApJ*, 416, 519

Carangelo, N., Falomo, R., Kotilainen, J., Treves, A., & Ulrich, M.-H. 2003, preprint (astro-ph/0306617), to be published in *A&A*

Cohen, M. H., et al. 1977, *Nature*, 268, 405

Dallacasa, D., Stanghellini, C., Centonza, M., & Fanti, R. 2000, *A&A*, 363, 887

Dermer, C. D., Schlickeiser, R., & Mastichiadis, A. 1992, *A&A*, 256, L27

Drinkwater, M. J., et al. 1997, *MNRAS*, 284, 85

Gomez, J.-L., Marscher, A. P., Alberdi, A., Jorstad, S. G., & Agudo, I. 2002, VLBA Scientific Memo No. 30, <http://www.aoc.nrao.edu/vlba/html/MEMOS/SCI/>

Homan, D. C., Ojha, R., Wardle, J. F. C., Roberts, D. H., Aller, M. F., Aller, H. D., & Hughes, P. A. 2002, *ApJ*, 568, 99

Hughes, P. A. 2005, *ApJ*, in press

Hughes, P. A., Aller, H. D., & Aller, M. F. 1985, *ApJ*, 298, 301

Table 5—Continued

Source (1)	r (2)	P.A. (3)	Maj. (4)	Ratio (5)	P.A. (6)	I (7)	<i>m</i> (8)	EVPA (9)
	1.22	290	0.61	1.00	...	60	4.8	232
	6.41	284	5.18	0.55	79	207	< 21.2	...

Note. — Columns are as follows: (1) IAU Name (B1950.0); (2) Distance from fitted core position (mas); (3) Position angle of component w.r.t. core position; (4) Major axis of fitted Gaussian (milliarcseconds); (5) Axial ratio of fitted Gaussian; (6) Position angle of major axis of fitted Gaussian; (7) log of brightness temperature (K); (8) Fitted component flux density (mJy); (9) Fractional polarization at component position; (10) Electric vector position angle at component position.

- Hughes, P. A., Miller, M. A., & Duncan, G. C. 2002, *ApJ*, 572, 713
- Jackson, C. A., Wall, J. V., Shaver, P. A., Kellermann, K. I., Hook, I. M., & Hawkins, M. R. S. 2002, *A&A*, 386, 97
- Jorstad, S. G., Marscher, A. P., Mattox, J. R., Wehrle, A. E., Bloom, S. D., & Yurchenko, A. V. 2001, *ApJS*, 134, 181
- Jorstad, S. G., Marscher, A. P., Mattox, J. R., Aller, M. F., Aller, H. D., Wehrle, A. E., & Bloom, S. D. 2001, *ApJ*, 556, 738
- Jorstad, S. G., et al. 2005, *ApJ*, submitted
- Kellermann, K. I., Vermeulen, R. C., Zensus, J. A., Cohen, M. H. 1998, *AJ*, 115, 1295
- Kellermann et al., 2004, *ApJ*, 609, 539
- Koide, S., Shibata, K., Kudoh, T., & Meier, D. L. 2002, *Science*, 295, 1688
- Kovalev, Y. Y., Kovalev, Y. A., Nizhelsky, N. A., & Bogdantsov, A. B. 2002, *Publications of the Astronomical Society of Australia*, 19, 83
- Kovalev, Y. Y., et al. 2005, *AJ*, submitted
- Kühr, H., Witzel, A., Pauliny-Toth, I. I. K., & Nauber, U. 1981, *A&AS*, 45, 367
- Lähteenmäki, A. & Valtaoja, E. 2003, *ApJ*, 590, 95
- Landt, H., Padovani, P., Perlman, E. S., & Giommi, P. 2004, *MNRAS*, 351, 83
- Lavalley, M., Isobe, T., & Feigelson, E. 1992, in *Astronomical Data Analysis Software and Systems I*, (PASP: San Francisco) eds. D. M. Worrall, C. Biemesderfer, & J. Barnes, 245
- Lind, K. R., & Blandford, R. D. 1985, *ApJ*, 295, 358
- Lister, M. L. 2001, *ApJ*, 562, 208
- Lister, M. L. & Marscher, A. P. 1997, *ApJ*, 476, 572
- Lister, M. L., Marscher, A. P., & Gear, W. K. 1998, *ApJ*, 504, 702
- Lister, M. L. & Smith, P. S. 2000, *ApJ*, 541, 66
- Lister, M. L., Tingay, S. J., & Preston, R. A. 2001, *ApJ*, 554, 964
- Lobanov, A. P. 1998, *A&A*, 330, 79
- Marscher, A. P., Jorstad, S. G., Mattox, J. R., & Wehrle, A. E. 2002, *ApJ*, 577, 85
- Mattox, J. R., Hartman, R. C., & Reimer, O. 2001, *ApJS*, 135, 155
- Moellenbrock, G. A., et al. 1996, *AJ*, 111, 2174
- Ochsenbein, F., Bauer, P., & Marcout, J. 2000, *A&AS*, 143, 23
- Perlman, E. S., Stocke, J. T., Carilli, C. L., Sugiho, M., Tashiro, M., Madejski, G., Wang, Q. D., & Conway, J. 2002, *AJ*, 124, 2401

- Shepherd, M. C., Pearson, T. J., & Taylor, G. B. 1994, *BAAS*, 26, 987
- Sowards-Emmerd, D., Romani, R. W., & Michelson, P. F. 2003, *ApJ*, 590, 109
- Sowards-Emmerd, D., Romani, R. W., Michelson, P. F., & Ulvestad, J. S. 2004, *ApJ*, 609, 564
- Stanghellini, C., O’Dea, C. P., Dallacasa, D., Baum, S. A., Fanti, R., & Fanti, C. 1998, *A&AS*, 131, 303
- Stickel, M., Meisenheimer, K., & Kühn, H. 1994, *A&AS*, 105, 211
- Stickel, M., Rieke, G. H., Kuehr, H., & Rieke, M. J. 1996, *ApJ*, 468, 556
- Taylor, G. B., Vermeulen, R. C., Readhead, A. C. S., Pearson, T. J., Henstock, D. R., & Wilkinson, P. N. 1996, *ApJS*, 107, 37
- Teräsranta, H., Urpo, S., Wiren, S., & Valtonen, M. 2001, *A&A*, 368, 431
- Urry, C. M. & Padovani, P. 1995, *PASP*, 107, 803
- Véron-Cetty, M.-P., & Véron, P. 2003, *A&A*, 412, 399
- Walker, R. C., Dhawan, V., Romney, J. D., Kellermann, K. I., & Vermeulen, R. C. 2000, *ApJ*, 530, 233
- Zavala, R. T., & Taylor, G. B. 2004, *ApJ*, 612, 749
- Zensus, A., Ros, E., Kellermann, K. I., Cohen, M. H., Vermeulen, R. C. 2003, *AJ*, 124, 662